Section 7

Global and regional climate models, sensitivity and impact experiments, response to external forcing

Response of permafrost to SRES A2 forcing in a climate model of intermediate complexity with a detailed soil module

M.M. Arzhanov, P.F. Demchenko, A.V. Eliseev, and I.I. Mokhov

A.M. Obukhov Institute of Atmospheric Physics RAS,
3 Pyzhevsky, 1191017 Moscow, Russia, e–mail: eliseev@ifaran.ru

The climate model of intermediate complexity developed at the A.M. Obukhov Insitute of Atmospheric Physics RAS (IAP RAS CM) [5] is extended by a detalied module for thermal and hydrological processes in soil [1, 2]. WIth the IAP RAS CM, a simulation is performed which is forced by the anthropogenic emissions of CO_2 and atmospheric concentration of CH_4, N_2O, and sulphate aerosols in accordance to historical data for the 19th-20th centuries and in accordance to scenario SRES A2 for the 21st century (more detailed description of these forcing scenarios is reported in [4].

The simulated area of the permafost extension varies little till the late 20th century varying in the range $20 - 21$ $mln\ km^2$ (Fig. 1). This value is between the estimated areas of the continious (10.7 $mln\ km^2$) and total (22.8 $mln\ km^2$). permafrost extensions [6]. Geographical distribution of the simulated permafrost (top panel in Fig. 2) is also realistic if compared with the empirical map from [6]. A notable exception is the region near the Baltic Sea where IAP RAS CM simulates permafrost absent in the observations.

In 21st century, permafrost cover shrinks rapidly. In the middle (late) 21st century the area of the permafrost extension attains the value 9 $mln\ km^2$ (2 $mln\ km^2$). (Fig. 1). The response in the second half of the 21st century is much stronger than obtained with the previous IAP RAS CM version [3]. To the middle of the 21st century, permafrost shrinks greatly in North America, and seasonal thaw depth increase drastically in Eurasia (middle panel in Fig. 2). To late 21st century, permafrost cover basically disappears in North America and shrinks about threefold in Eurasia (bottom panel in Fig. 2). In the latter case, typical thaw depth is larger than 2 m.

This work was supported by the Russian Foundation for Basic Research, by the programs of the Russian Academy of Sciences, and by the Russian President scientific grant.

References

[1] M.M. Arzhanov, A.V. Eliseev, P.F. Demchenko, and I.I. Mokhov. Modelling of temperature and hydrological changes in subsurface permafrost by using climate data (reanalysis). *Earth's*

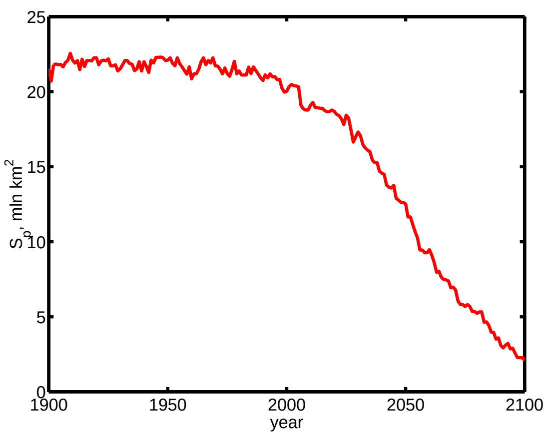

Figure 1: Area of the permafrost extension simulated by IAP RAS CM.

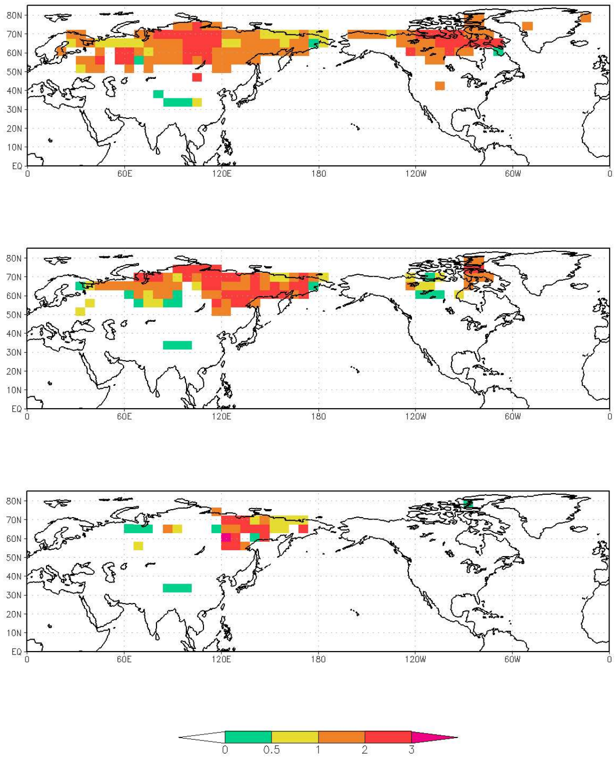

Figure 2: Mean seasonal thaw depth (meters) in the Northern hemisphere simulated by IAP RAS CM for 1961–2000, 2035–2065, and and 2071–2100 (top, middle, bottom panels respectively) under the SRES A2 forcing scenario.

Cryosphere, XI(4), 2007.

[2] M.M. Arzhanov, A.V. Eliseev, P.F. Demchenko, I.I. Mokhov, and V.Ch. Khon. Modelling of temperature and hydrological over the siberian rivers watersheds in presence of permafrost by using the reanalysis data. *Izvestiya, Atmos. Ocean. Phys.*, 44(1), 2008. [in press].

[3] A.V. Eliseev, I.I. Mokhov, M.M. Arzhanov, P.F. Demchenko, and S.N. Denisov. Accounting interaction between methane cycle and processes in wetlands in a climate model of intermediate complexity. *Izvestiya, Atmos Ocean Phys.*, 44(2), 2008. [in press].

[4] A.V. Eliseev, I.I. Mokhov, and A.A. Karpenko. Influence of direct sulfate–aerosol radiative forcing on the results of numerical experiments with a climate model of intermediate complexity. *Izvestiya, Atmos. Ocean. Phys.*, 42(5):544–554, 2007.

[5] I.I. Mokhov, V.A. Bezverkhnii, A.V. Eliseev, and A.A. Karpenko. Model estimates of global climatic changes in the 21st century with account for different variation scenarios of solar activity. *Doklady Earth Sci.*, 411(8):1327–1330, 2006.

[6] T. Zhang, R.G. Barry, K. Knowles, J.A. Heginbottom, and J. Brown. Statistics and characteristics of permafrost and ground–ice distribution in the Northern Hemisphere. *Polar Geogr.*, 23(2):132–154, 1999.

Using Isotopes and an Observational Based Regression Model to Assess the Hydrological Cycle in GCMs

Nikolaus Buenning[1], David Noone[1]

[1] Cooperative Institute of Research in Environmental Sciences and the Department of Atmospheric and Oceanic Sciences, University of Colorado, Boulder, CO, USA

(Email: buenning@colorado.edu)

The isotopic composition of precipitation (herein after denoted as δ, where $\delta = (R/R_{STANDARD} - 1) \times 1000$, and R is the heavy to light isotope ratio, and we focus here on the oxygen-18 in precipitation, $\delta^{18}O$) is widely used for both hydrology and climate variability studies. Mapping out the spatial distribution of δ values has been done by several studies using regressions (e.g. Farquhar et al., 1993; Bowen and Wilkinson, 2002; Buenning and Noone, 2008). Isotope equipped General Circulation Models (GCMs) provide another approach in predicting the spatial distribution of δ values. In this study, regressions are performed on both the Global Network for Isotopes in Precipitation (GNIP) observational records and three GCMs to examine how well the models capture the balance of local and non-local (advective) controls. This type of analysis provides a measure of which processes give rise to model errors, and thus expands on simple model/data comparisons. In particular, the models have large errors over the high-latitudes, where predicted δ values are not depleted enough; a regression analysis provides insight into why the models perform poorly in these regions. The regression model used here is one that is similar to both Farquhar et al. (1993), Bowen and Wilkinson (2002), and described in detail by Buenning and Noone (2008):

$$\delta_a = a_1 T + a_2 T^2 + a_3 P + a_4 |\phi| + a_5 \phi^2 + a_6 \theta + a_7 \theta^2 + a_8$$

where T is annual mean temperature (K), P is annual mean precipitation (mm month^{-1}), is the latitude, θ is annual mean potential temperature (K), and a values are regression coefficients used to fit the observed and simulated $\delta^{18}O$ values. The regression is performed on the GNIP station observations as well as the GCMs. The GCMs examined here are MUGCM, ECHAM, and GISS, using simulated δ, T, P and θ fields. The regression bias, associated with processes not captured by the local conditions (both observed and simulated), is defined as $\varepsilon = \delta_a - \delta_o$ where δ_o is the observed or simulated value.

Figure 1a shows the annual mean bias of the observational based regression for $\delta^{18}O$ values, mapped onto a grid using Cressman (1959) objective analysis. The regression model bias has a root mean square error of 2.26‰. However, has large biases at certain locations. For instance, the regression predicts the δ values to be too low over the Southern Oceans and the Arctic Ocean north of Scandinavia. Over most of Canada and Alaska, the model predicts δ values that are not depleted enough.

These locations are consistent with the regions where Bowen and Wilkerson (2001) found high-magnitude residual regions. Many of the problematic regions were in the mid and high latitudes, and were due to differences in vapor transport within the latitudinal zones. For example, vapor in the North Atlantic (where temperatures are high) is advected northeastward towards the Arctic Ocean where the resulting rain will be enriched in the heavy isotopes compared to other locations within a latitudinal zone. Over Canada, the opposite occurs as vapor is transported from the northwest, bringing in more depleted δ values.

Using simulated values from GCM grid cells, comparable GCM-based regression models were established, and the bias relative to the GCM simulated $\delta^{18}O$ are computed (Figures 1b-d).

Many of the biases that appeared in the observationally based regression model also show up in the GCMs; however, the magnitudes and extent are different in some regions. For example, all of the regression biases are large and positive in northern Canada; though, the GCM-based biases are higher in the eastern portion of the continent and are generally large throughout the high and mid northern latitudes. This would indicate that the GCMs inadequately simulate the non-local controls of the hydrological cycle for the northern continents. Furthermore, the observational and GCM based regressions all have negative biases in the Southern Oceans. This would suggest that the δ values are largely influenced by non-local process for this region, such as moisture advection, and the GCMs reasonably capture this non-local component of the hydrological cycle. However, the extent and magnitude of this bias is much greater than the observational-based regression (with the exception of the regions adjacent to Africa). Similarly, there is region in the Arctic Ocean, north of Scandinavia that also has large negative bias for both the observational based and GCM based regressions. Thus, the GCMs are able to capture the balance between local and non-local processes in the hydrological cycle in a bulk sense, but there are large regions within the mid to high latitudes where model improvements are needed.

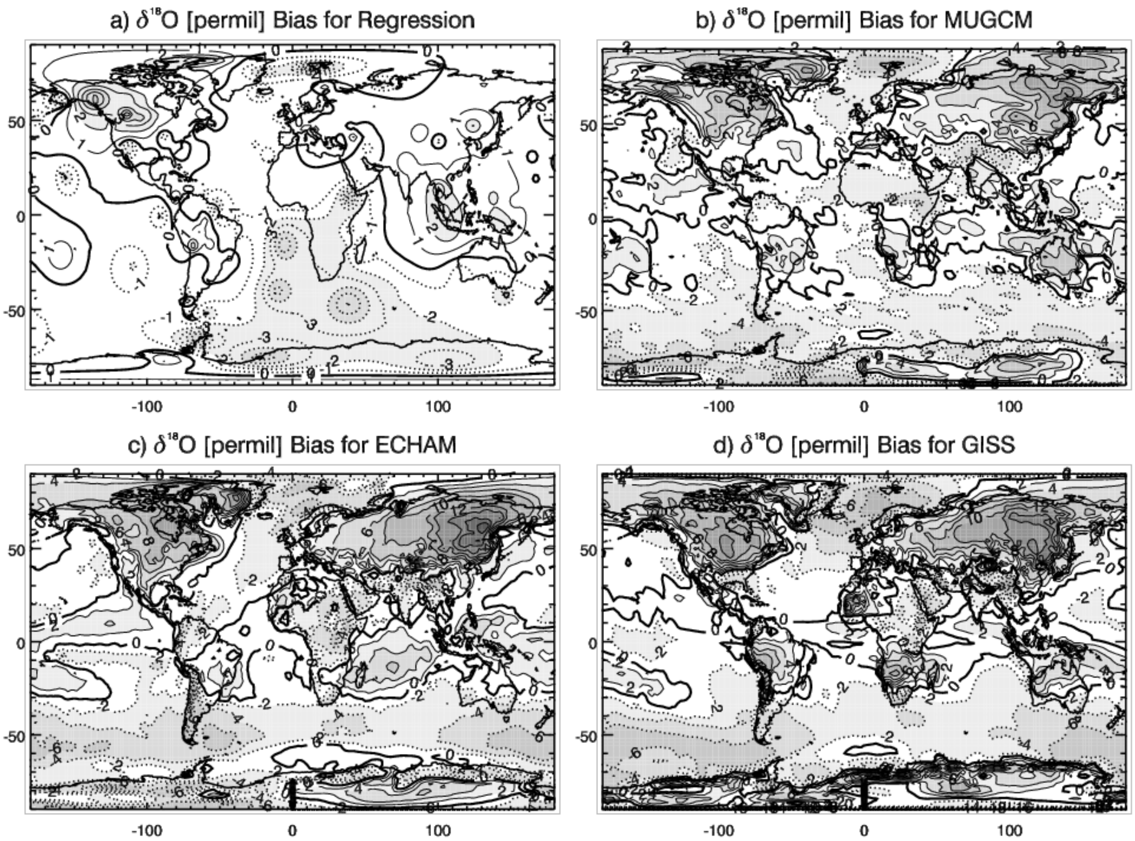

Figure 1. Annual mean δ^{18}O bias (‰) for regressions based on (a) observations (interpolated to a grid), and results from (b) MUGCM, (c) ECHAM, and (d) GISS

Bowen, G. J., and B. Wilkinson, Spatial distribution of d18O in meteoric precipitation, *Geology*, **30**, 315-318, 2002.

Buenning, N. and D. Noone., Modeling the spatial and temporal variations in the isotopic composition of precipitation with statistical and dynamical methods, 2008 (in preparation)

Cressman, G. P., An operative objective analysis system, *Mon. Weather Rev.*, **87**, 367-374, 1959.

Farquhar, G. D., J. Lloyd, J. A. Taylor, L. B. Flanagan, J. P. Syvertsen, K. T. Hubick, S. Wong, and J. R. Ehleringer,. Vegetation effects on the isotope composition of oxygen in atmospheric CO_2, *Nature* **363**, 439-443, 1993.

Simulating High-Resolution Atlantic Tropical Cyclones with GEM-Climate

Louis-Philippe Caron[1] Colin G. Jones[1] Katja Winger[1]
[1] *Université du Québec à Montréal, CRCMD Network*
emails: lpcaron@sca.uqam.ca, jones.colin@uqam.ca, katja.winger@ec.gc.ca

Since 1995, tropical cyclone (TC) activity in the Atlantic has increased markedly in contrast to the quieter period of the 1970's and 1980's. The recent years have seen many records broken in the Atlantic, such as the largest number of tropical cyclones in a given season and the most powerful storm ever recorded. As well, the accumulated cyclone energy index has been above the 1951-2000 median for all years from 1995-2005, except in 1997 and 2002 (Bell and Chelliah, 2006), years during which an El-Niño, known to suppress TC activity in the Atlantic, was observed. Whether this upswing in activity is due to a multi-decadal natural variability, to a long-term rising trend caused by anthropogenically forced global warming or to a combination of the two is still unclear. This uncertainty has its root in the relatively limited number of years of hurricane data available and the reliability of these historical data.

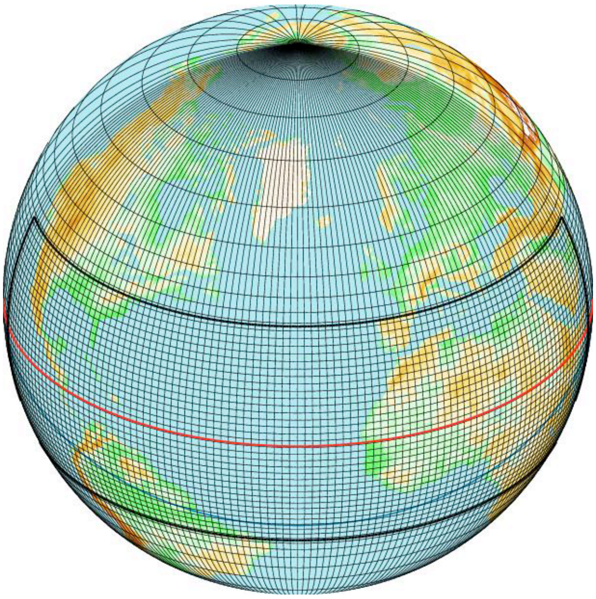

Figure 1: Variable resolution grid used in this study.

Climate models offer an alternative by which to explore TC activity and the factors controlling interannual variability. However, so far, Global Climate Model (GCM) studies of future TC activity have shown widely different conclusions. One major cause of this is the low resolution of GCMs and their inability to simulate the important processes controlling TC genesis and intensification. The physical realism of these simulated TCs improves with increasing model resolution. Running a high-resolution model (20-30 km) over the whole globe is presently not feasible except on the most powerful supercomputers currently available. An alternative approach to achieving locally enhanced resolution (e.g. over the tropical Atlantic) to study resolution benefits on TC simulation is to run a GCM in variable resolution mode, whereby resolution is locally increased within a predefined region of the continuous global domain. In this study, we exploit this variable resolution option in the Global Environmental Multiscale (GEM) model (Côté et al., 1998) using a 2° global domain with telescoping up to 0.3° over the entire tropical Atlantic TC tracks (figure 1).

Initially, we concentrate on the ability of GEM to simulate past observed Atlantic TC activity. In the first step of this evaluation, GEM in variable GCM mode (GVAR) has been integrated for the period 1979-2004 using observed sea surface temperatures (SSTs). Simulated TCs were identified according to a scheme suggested by Walsh et al. (2007). Accordingly, a TC is detected if a system displays for 24h the following characteristics:

- a minimum pressure in the center.
- surface winds of at least 17 $m\ s^{-1}$ (65 $km\ h^{-1}$) in the vicinity of the center.
- a warm core in the mid- to upper-troposphere.

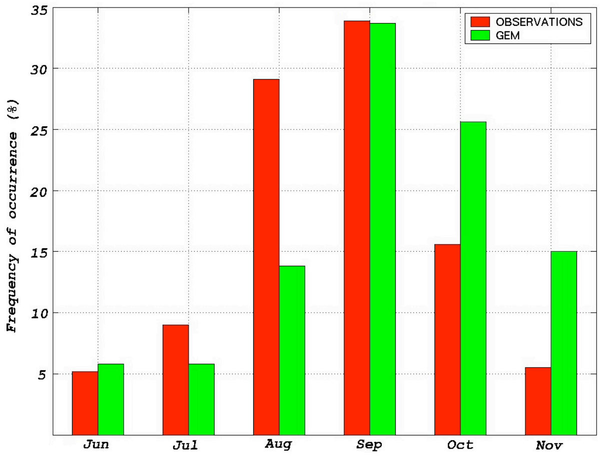

Figure 2: Relative monthly distribution of Atlantic tropical cyclones, 1979-2004.

Results

A comparison of simulated TC activity between the GVAR run and observations allows a direct comparison of TC statistics on climate timescales. For example, the majority of Atlantic tropical storms are observed from August to October. Figure 2 shows the relative monthly distribution of TC formation for the period 1979-2004 for both observed and simulated tropical storms. We notice that GEM reproduces fairly well the intra-annual distribution of TCs, with a maximum during the peak of hurricane season (September). However, its overall distribution is biased toward a too large proportion of TCs at the end of the year to the detriment of the beginning of hurricane season. In absolute numbers, GEM tends to systematically overestimate the monthly production of TCs; the reasons as to why this is the case are currently under investigation.

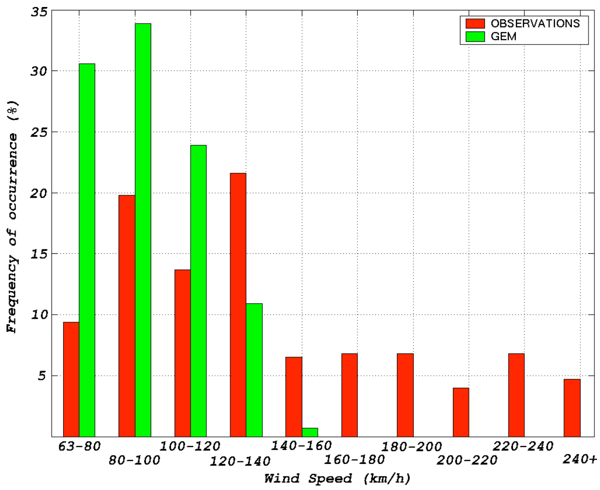

Figure 3: Relative wind speed distribution of Atlantic tropical cyclones, 1979-2004.

A recurrent problem with low-resolution GCMs when studying TCs is the low intensity of the system produced: GCMs produce systems that are reminiscent of TCs, but which are too weak to be considered so. The wind speed threshold of 65km/h is rarely reached with low-resolution GCM. By increasing the resolution to 0.3°, we witness the formation of tropical storms and category 1 hurricanes (threshold of 119km/h). Figure 3 shows that GEM comes short of producing the most intense storms (Cat 3+); further increases in resolution seem to be necessary for detecting these most destructive storms. This is not entirely surprising since 0.3° appears insufficient resolution for eye development, a key process to reaching very high wind speed.

References:

Bell, G.D. and M. Chelliah, 2006: Leading tropical modes associated with interannual and multidecadal fluctuations in North Atlantic hurricane activity. *J. Climate*, **19**, 590-612.

Côté J., S. Gravel, A. Methot and coauthors, 1998: The operational CMC/MRB Global Environmental Multiscale (GEM) model: Part I - Design considerations and formulation. *Mon. Wea. Rev.*, **126**, 1373-1395.

Walsh, K. J. E., M. Fiorino, C. W. Landsea, and K. L. McInnes, 2007: Objectively Determined Resolution-Dependent Threshold Criteria for the Detection of Tropical Cyclones in Climate Models and Reanalysis. *J. Climate*, **20**, 2307-2314.

Forest fire conditions in Eurasian regions from model simulation

Chernokulsky A.V. and Mokhov I.I.
A.M. Obukhov Institute of Atmospheric Physics RAS, Moscow, Russia
chern_av@ifaran.ru

Forest fires are one of the most hazardous regional consequences of global warming of the climate. Fire conditions can be characterized by indices based on meteorological data, including the Nesterov fire index (Nesterov 1949), Zhdanko index (Zhdanko, 1964), modified Nesterov index (Groisman et al, 2007). In particular, Nesterov fire hazard index (*FHI*) is defined as:

$$FHI = \sum_{P>3mm} \left(T_{\max} - T_{dew}\right) \cdot T_{\max},$$

where $T_{\max}$ is the maximal temperature in °C and T_{dew} is the temperature of the dew-point (depending on relative humidity and temperature) in °C. Summation is performed for those days when the daily precipitation P does not exceed 3 mm. At P>3mm, the FHI value turns to zero. The values of fire hazard potential are divided into five ranges. Conditions with $FHI < 300$ (regime I) are not considered hazardous. Conditions in the ranges 300–1000, 1000–4000, 4000–10000, and >10000 are considered regimes with low (II), moderate (III), high (IV), and extreme (V) level of fire hazard.

In the present paper, we estimate the regimes of fire hazard in North Eurasian regions at the end of 20st century and during possible climate changes in the 21st century based on numerical calculations using MGO regional climatic model (Shkolnik et al., 2006, 2007).

Figures 1 and 2 show distributions of the mean summer FHI for the European and Asian part of Russia for the period 1991–2000. Southern latitudes are generally characterized by extreme FHI values. Boundaries of the regions with forests were distinguished according to satellite data (Hansen et al., 2000). Southern boundary of the regions with forests is associated with regime III with moderate FHI values. Remarkable exception is related with the Siberian region to the east from Baikal Lake. There forest zone locates in regime IV with high level of fire hazard.

Forests in midlatitudes are associated mainly with low FHI conditions (regime II) as well for high latitudes over European part of Russia (Fig. 1).

We analyzed also simulations for 2041-2050 and for 2091-2100 periods under the SRES-A2 scenario (Mokhov, et al, 2006). Tendencies of change for summer precipitation differ in sign in the northern and southern latitudes. Differences in the temperature changes are not so dramatic for different regions. Regional temperature changes differ only in their value but not in sign: they are generally positive in the 21st century according to model simulations. The combination of change in temperature and hydrological characteristics leads to a general increase in fire indices for south regions in Northern Eurasia by the end of the 21st century in particular to the east from Baikal Lake in Siberia.

This work was partly supported by the Russian Foundation for Basic Research, by the Programs of the Russian Academy of Sciences and by the Russian President scientific grant.

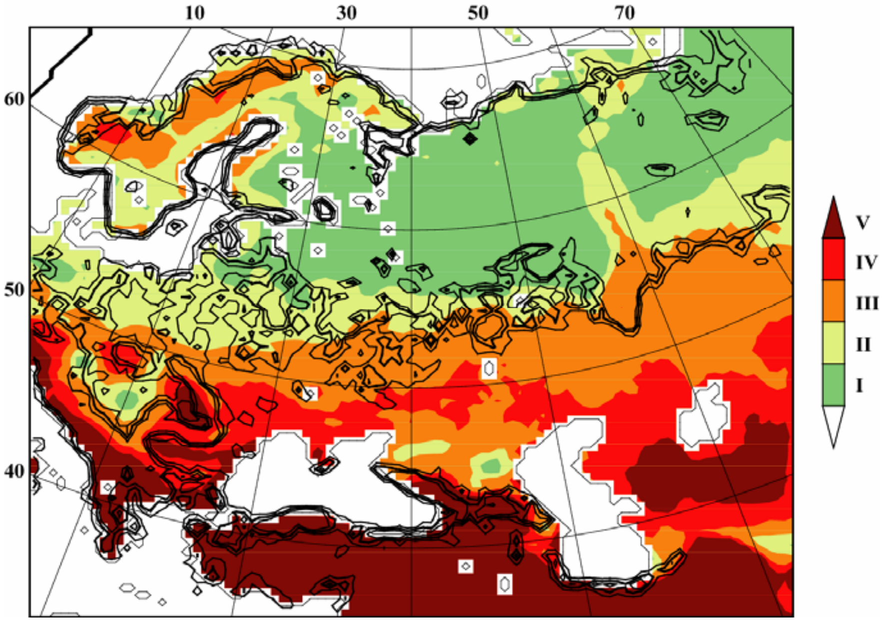

Fig.1 Distribution of the mean summer *FHI* for the terminal 20th century at the European part.

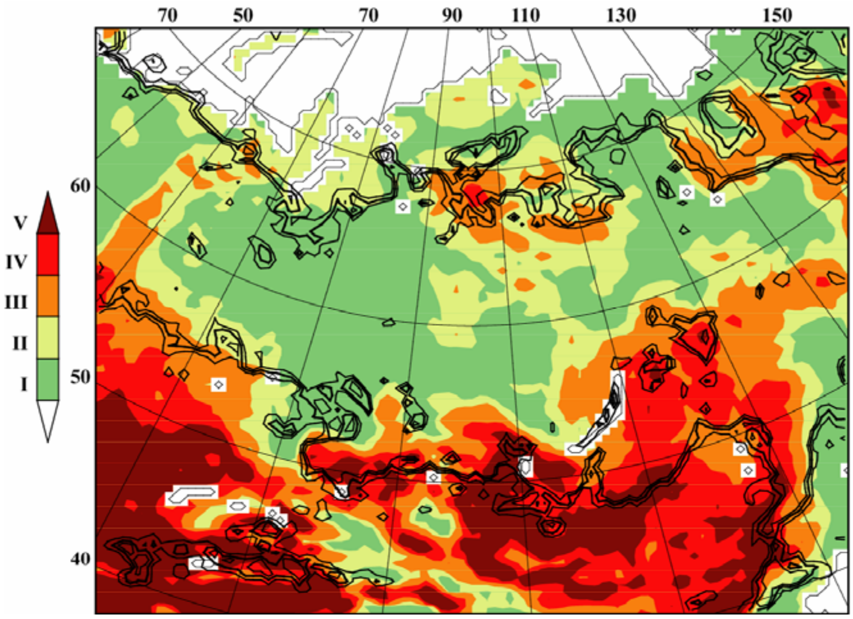

Fig.2 Distribution of the mean summer *FHI* for the terminal 20th century at the Asian part.

References

Groisman P. Ya., B.G. Sherstyukov, V.N. Razuvaev, R.W. Knight, J.G. Enloe, N.S. Stroumentova, P.H. Whitfield, E. Førland, I. Hannsen-Bauer, H. Tuomenvirta, H. Aleksandersson, A.V. Mescherskaya, T.R. Karl. Potential forest fire danger over Northern Eurasia: Changes during the 20th century. *Global and Planetary Change*, 2007, 56, 371–386.

Hansen, M., R. DeFries, J.R.G. Townshend, and R. Sohlberg. Global land cover classification at 1km resolution using a decision tree classifier. *International Journal of Remote Sensing*. 2000, 21, 1331-1365.

Mokhov I.I., A.V. Chernokulsky, I.M. Shkolnik. Regional model assessments of fire risk under global climate changes. *Doklady Earth Sciences*, 2006, 411A, 9, 1485-1488

Nesterov V.G. Gorimost' lesa I metody ee opredelenia, Moscow, Goslesbumaga, 1949 [in Russian]

Shkolnik, I. M., V. P. Meleshko, and V. M. Katsov. Possible climate change in European part of Russia and contiguous territories to the end of the 21st century: Simulation with the MGO regional model. *Meteorol. Hydrol.*, 2006, 3, 5-16.

Shkolnik, I. M., V. P. Meleshko, and V. M. Katsov. MGO regional climate model for Siberia region. *Meteorol. Hydrol*, 2007, 6, 5-18.

Zhdanko, V.A. Scientific basis of development of regional scales and their importance for forest fire management. In: Melekhov, I.S. (Ed.), Contemporary Problems of Forest Protection from Fire and Firefighting. Lesnaya Promyshlennost' Publ.,Moscow, 1965, 53–86 [in Russian]

Geoengineering efficiency: Preliminary assessment for year 2100 with an energy-balance climate model

A.V. Chernokulsky, A.V. Eliseev and I.I. Mokhov
A.M. Obukhov Institute of Atmospheric Physics RAS, Moscow, Russia
chern_av@ifaran.ru

One of the possible solution of global warming is a loading sulphur particles in the stratosphere to enhance the Earth's albedo (Budyko, 1974) recently entitled as geoengineering (Izrael, 2005; Crutzen, 2006; Wigley, 2006; Mokhov and Eliseev, 2008). In the present paper, we estimate geoengineering efficiency by using an energy-balance climate model.

The governing equation for globally averaged model reads

$$C\frac{dT}{dt} = S(1-\alpha_A(T)) - (A+BT)\eta_C(q) - F_{strat}\,, \tag{1}$$

where T is globally and annually averaged surface air temperature, C is heat capacity per unit area, t is time, S is one quarter of the insolation at the top of the atmosphere, α_A is planetary albedo, A and B are coefficients of the linear dependence of outgoing longwave radiation (OLR) on temperature (Budyko, 1974), $\eta_C = 1 - c_0 \ln\frac{q(t)}{q_0}$ is OLR greenhouse correction factor, q is CO_2 atmospheric content, q_0 is its initial value, $c_0 = 1{,}4\cdot 10^{-2}$ (Mokhov, Petukhov, 1978), F_{strat} is mitigation geoengineering forcing. In the linearised setting, this model has a solution which can be represented as a sum of two responses, one due to greenhouse forcing and another due to geoengineering mitigation:

$$T = T_C + T_{strat}\ . \tag{2}$$

If the buildup of greenhouse gases in the atmosphere (being expressed via "effective CO_2" (IPCC, 2001)) has an exponential form: $q = q_0\cdot\exp(t/t_p)$, (t_p is time scale of CO_2 atmospheric content change), then the solutions are:

$$T_C = -\frac{\Delta T_{2xCO_2}}{t_p \ln 2}\left(\frac{1}{p}(e^{pt}-1) - t\right) \tag{3}$$

$$T_{strat} = \frac{1}{p}\left(-\frac{a\cdot k_e M_{strat}}{4\pi R^2 C}\right)(e^{pt}-1)\ . \tag{4}$$

In Eq.(3), ΔT_{2xCO_2} is equilibrium model's response to the doubling of CO_2 in the atmosphere, and $p = -\frac{S(1-\alpha_A)c_O \ln 2}{C\cdot\Delta T_{2xCO_2}}$. Eq.(4) is obtained assuming that stratospheric aerosol mass is equilibrated, normaly, $M_{strat} = E_{strat}\cdot t_{strat}$. Here, E_{strat} stands for geoengineering emission and t_{strat} is lifetime of stratospheric aerosols, k_e is a coefficient of extinction of stratospheric sulphur aerosol (it's equal 7.6m^2/gS).

With this model, an ensemble simulation is performed with E_{strat} is varied between 0.6 MtS/yr (Izrael, 2005) up to 5 MtS/yr (including values 1-2 TgS/yr as suggested by Crutzen (2006) and Wigley (2006)) but kept independent on time, t_{strat} is varied in the range 1-4 yr, t_p is varied from 50 yr to 250 yr, and ΔT_{2xCO_2} is varied in the range 1.5-4.5 K which is slightly wider than the range figured in (IPCC, 2007).

Without a geoengineering mitigation, at the end of 21st century temperature changes by 0.5-14.0°C depending on the model parameters (Fig.1).

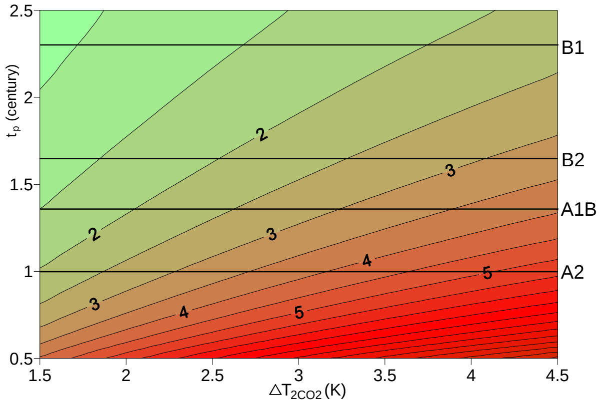

Fig.1 Temperatures changes in year 2100 without a geoengineering mitigation. The time scales corresponding to the SRES scenarios (taking into account CO_2, CH_4, and N_2O under the "effective CO_2" approximation) (IPCC, 2001) are depicted by horizontal lines.

Fig.2 Temperatures changes in year 2100 with a geoengineering mitigation for E_{strat} =1.0 MtS/yr (left) and E_{strat} =4.0 MtS/yr (right).

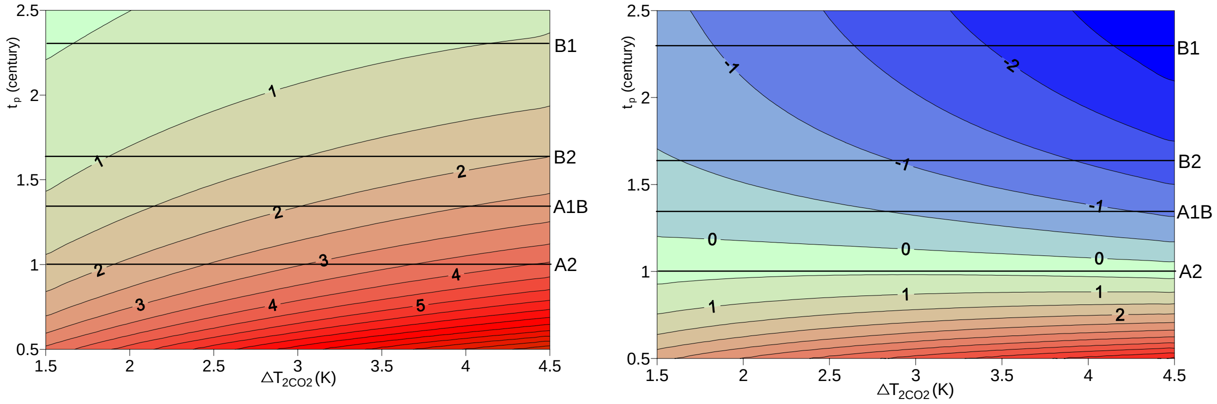

According to obtained results, it is possible to slow down current anthropogenic warming by applying a geoengineering approach (Fig.2). This mitigation is very efficient (and even excessive) if geoengineering emissions and/or life time of sulphates in the stratosphere are large enough and, additionally, the CO_2 atmospheric buildup is not too rapid. However, for E_{strat} from the lower part of the studied range, the residual warming is still substantional, especially for the scenarios with small t_p (e.g., for the SRES A2 and A1B scenarios).

This work is supported by the Russian Foundation for Basic Research, by the programs of the Russian Academy of Sciences, and by the Russian President scientific grant.

References

M.I. Budyko. *Climate Changes*. Gidrometeoizdat, Leningrad, 1974. [English transl. published in 1977 by the American Geophysical Union, Washington, D.C.].

Climate Change 2001: The Scientific Basis, IntergovernmentalPanel on Climate Change, Ed. by J. T. Houghton, *et al.* Cambridge Univ. Press,Cambridge, 2001.

Climate Change 2007: The Physical Science Basis. Contribution of Working Group I to the Fourth Assessment Report of the Intergovernmental Panel on Climate Change, Ed by S. Solomon, *et al.* Cambridge University Press, Cambridge, 2007.

P.J. Crutzen. Albedo enhancement by stratospheric sulfur injections: A contribution to resolve a policy dilemma? *Clim. Change*, 77(3-4):211–219, 2006.

Yu.A. Izrael. An efficient way to regulate global climate is the main goal of the climate problem solution. *Rus. Meteorol. Hydrol.*, 30(10):1–4, 2005.

I.I. Mokhov and A.V. Eliseev Geoengineering efficiency: Preliminary assessment with a climate model of intermediate complexity *Research Activities in Atmospheric and Oceanic Modelling*, J. Cote (ed.). 2008, this volume.

I.I. Mokhov and V.K. Petukhov. *Parameterization of outgoing longwave radiation for climate models*. Institute of Atmospheric Physics, USSR Academy of Sciences, 1978, [in Russian].

T.M.L. Wigley. A combined mitigation/geoengineering approach to climate stabilization. *Science*, 314(5798):452–454, 2006.

Evaluation of changes in methane emissions by wetlands of the European and Asian parts of Russia in the 21th century based on regional climate model simulations.

S.N. Denisov, A.V. Eliseev, I.I. Mokhov

A.M. Obukhov Institute of Atmospheric Physics RAS, Moscow, Russia
denisov@ifaran.ru

Module of methane emissions based on [1] was developed for the climate model of intermediate complexity of the A.M. Obukhov Institute of Atmospheric Physics RAS (IAP RAS CM). Previous simulations with this module were performed with use of data of relatively coarse spatial resolution [3,4]. In present work, a simulation with module of methane emissions is performed using the MGO regional climate model simulations data for the 21th century [5] with high spatial resolution. A simulation is forced by temperature and fractional saturation of soil layers and performed only for regions with porosity higher than 0.4 which is the evidence of presence of peat in the soil.

Simulations was performed for the European and Asian parts of Russia (Fig. 1). Simulated methane emissions for the present day period (1991-2000) amount about 8 $MtCH_4$/yr for the European part of Russia and 10 $MtCH_4$/yr for the Asian part (Fig. 2). Geographical distribution of the simulated methane emissions is realistic as a whole if compared with map [2]. A notable exceptions is the region near Baltic Sea where simulated emissions are low and the southern part of eastern Europe where emissions absent in observations.

Simulated emissions increase up to 11 for the European part of Russia and 13 $MtCH_4$/yr for the Asian part to the middle of the 21th century, and up to 14 and 17 $MtCH_4$/yr to its end, respectively (Fig. 3). These tendencies are related to the increase of thaw period in soil and integral methane production dependence on temperature.

This work is supported by the Russian Foundation for Basic Research, by the programs of Department of Earth Sciences of the Russian Academy of Sciences, and by the Russian President scientific grant.

References

[1] T.R. Christensen and P. Cox. Response of methane emission from arctic tundra to climatic change: results from a model simulation. *Tellus*, 47B(3):301-309, 1995.

[2] E. Matthews, I. Fung. Methane emissions from natural wetlands: Global distribution, area and environmental characteristics of sources. *Glob. Biogeochem. Cycles*, V. 1, P. 61-86, 1987.

[3] I.I. Mokhov, A.V. Eliseev, S.N. Denisov. Model diagnostics of variations in methane emissions by wetlands in the second half of the 20th century based on reanalysis data. *Doklady Earth Sciences*, V. 417, N. 8, P. 1293-1297, 2007.

[4] A.V. Eliseev, I.I. Mokhov, M.M. Arzhanov, P.F. Demchenko, S.N. Denisov. The account of interaction of a methane cycle and processes in wet ecosystems in climatic model of intermediate complexity. *Izvestia, Atmos. Oceanic Phys*., 44 (2), 1-15, 2008. [in Russian]

[5] I.M. Shkolnik, V.P. Meleshko, V.M. Katzov. Possible changes of a climate on the European part of Russia and adjacent territories by the end of the 21th century: simulations with MGO regional model. *Meteorol. Hydrol*., (3), 5-16, 2006.

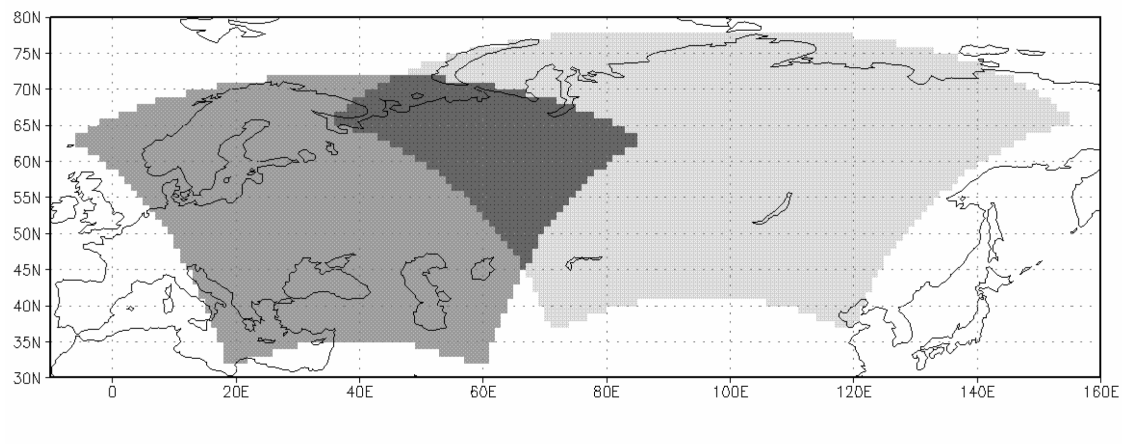

Figure 1: European and Asian parts of Russia in regional climate model.

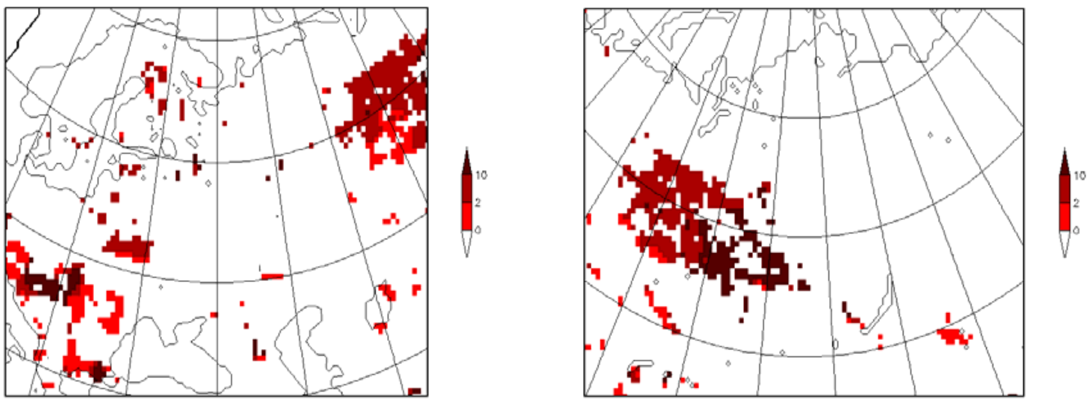

Figure 2: Modelled methane emissions ($g \cdot m^{-2} yr^{-1}$) in the end of the 20th century.

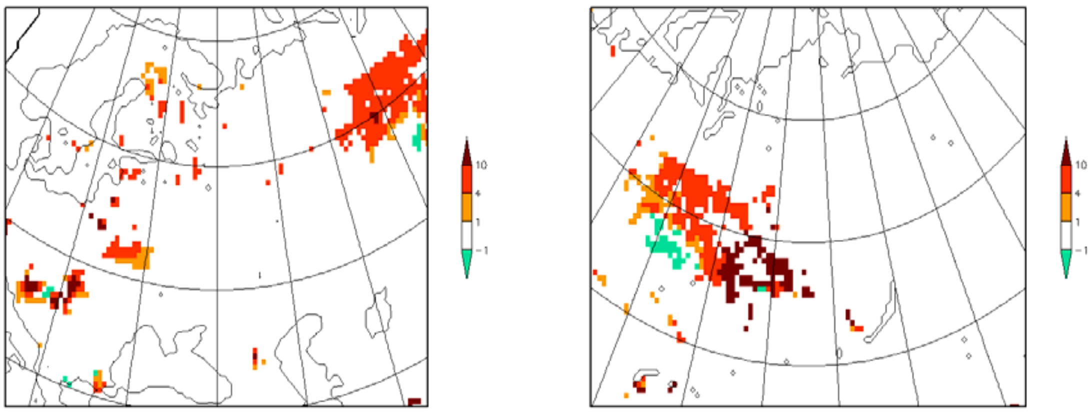

Figure 3: Changes in simulated methane flux ($g \cdot m^{-2} yr^{-1}$) from the end of 20th century to the end of 21th.

Modelling regional climate change in Eastern Africa on orbital and tectonic time scales

Frank Kaspar[1,2], Ulrich Cubasch[1]

[1]Institute for Meteorology, Freie Universität Berlin, Carl-Heinrich-Becker-Weg 6-10, 12165 Berlin, Germany, frank.kaspar@met.fu-berlin.de; [2]now at: Satellite Application Facility on Climate Monitoring (CM-SAF), Deutscher Wetterdienst, Offenbach, Germany

Orbital and tectonic forcing

On time scales of the last millions of years, two factors are assumed to be the major driving forces of climate change: Orbital forcing is assumed to be responsible for the cycles of glacial and interglacials. Data from ice cores indicate that interglacials occurred with a frequency of around 100,000 years at least during the last 500,000 years. Time scales of tectonically induced climate changes are typically an order of magnitude longer. The German interdisciplinary research group RiftLink (www.riftlink.de) analyses the interrelation between tectonics, climate change and human evolution in East Africa. One potential reason for the aridification of this region is the change in local topography due to tectonic uplift in the East African Rift System (Sepulchre et al., 2006). In the contribution of the Institute for Meteorology (Freie Universität Berlin) climate models are applied to analyse the role of different forcing factors. Two categories of models are applied: Coupled global ocean-atmosphere models are used to compare the effects of different driving forces that act on the global scale, mainly orbital and tectonic forcing. Regional climate models are used to analyse smaller scales effects of the complex East African topography. Here we present examples for both types of model applications.

Results of global modelling experiments: Orbital vs. tectonic forcing

In a first experiment, we used the global coupled ocean-atmosphere model ECHO-G and removed the topography of East and South Africa almost completely according to the set-up suggested by Sepulchre et al. (2006). A simulation with pre-industrial conditions is used for comparison. The climate model ECHO-G consists of the ECHAM4 atmosphere model at a spatial resolution of ~3.75° (19 vertical level) coupled to the HOPE-G ocean model at a resolution of ~2.8° (Legutke and Voss; 1999).Figure 1 illustrates the simulated effects on moisture transport during Northern Hemispheric summer (JJA). The results indicate that modifications in the topography lead to distinct change in moisture transport into the continent. The removal of the topographic barrier leads to an enhanced zonal moisture transport, e.g. stronger westward transport in the region between 15°S and 5°S during summer. This is consistent to the results of Sepulchre et al. (2006). As an example for other forcing factors, Figure 1 also shows equivalent results for the Eemian interglacial (125,000 years BP). In that case changes in Earth‘s orbital configuration lead to enhanced moisture transport from the Atlantic deep into the African continent in the region between 5°N to 10°N.

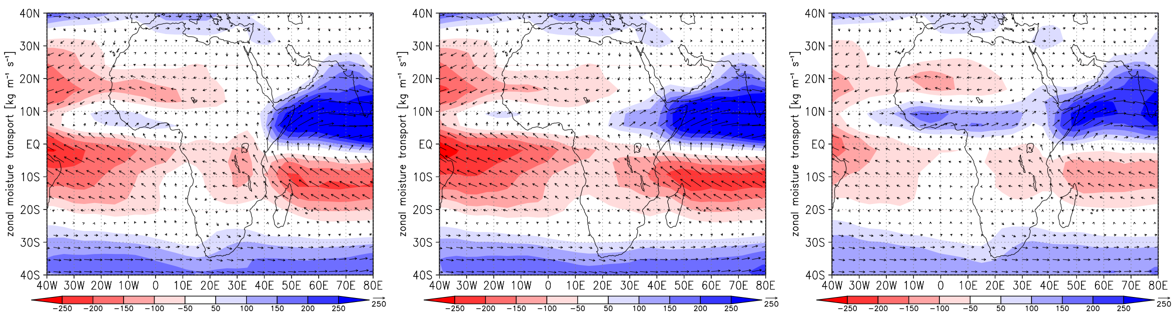

Figure 1: Vertically integrated moisture transport for northern hemispheric summer (JJA) for different forcings: (left): pre-industrial, (mid): with significantly reduced topography, (right) Eemian interglacial

Application of the regional climate model COSMO-CLM to East Africa

Applications of regional climate model to Eastern Africa are sparse (Sun et al.,1999a; Anyah and Semazzi, 2007). Here we apply the non-hydrostatic regional climate model COSMO-CLM (see: www.clm-community.eu), that is derived from the local weather prediction model of the German meteorological service (DWD). As first test case, the model is driven with ERA40 reanalysis in order to analyse its ability to realistically simulate present-day climate of that region. Figure 2 shows a comparison of simulated precipitation and observed data (GPCC) for the 'short rains season' (October to December). The figure shows results of model configurations with two different convection scheme (following Tiedtke (1989) and Kain and Fritsch (1993)). Overall, relatively good agreement with observed precipitation is achieved in a configuration with the 'Tiedtke'-convection scheme and a two category cloud ice scheme (see Kaspar and Cubasch (2008) for more details). This configuration is also used in operational weather prediction. As next step, the model will be driven by boundary conditions from the above mentioned ECHO-G simulations. An example driven by the pre-industrial ECHO-G simulation is also included in Figure 2.

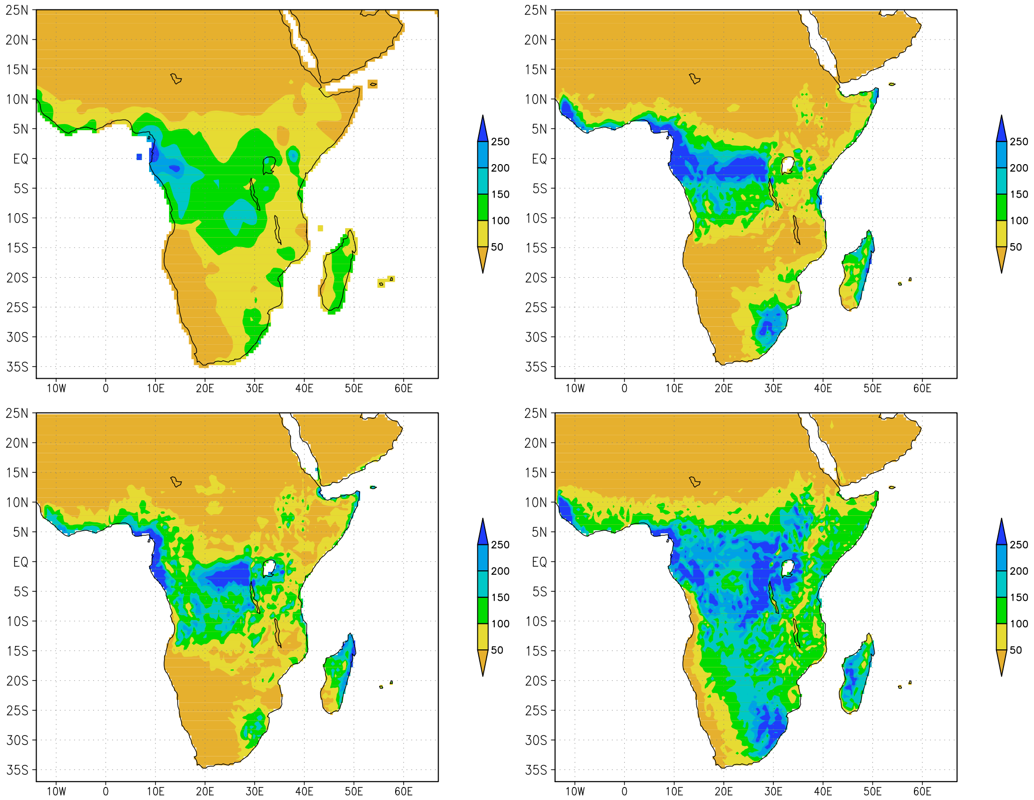

Figure 2: Precipitation of the short rains season (Oct.-Dec.): (top, left): GPCC observation, (top, right): simulated by COSMO-CLM with ERA 40 boundary conditions, Tiedtke convection scheme and two-category cloud ice scheme, (bottom, left): as before but with boundary conditions from a pre-industrial ECHO-G simulation (bottom, right): as (top, right) but with Kain-Fritsch scheme.

Anyah, R. O.; Semazzi, F. H. M.: Variability of East African rainfall based on multiyear RegCM3 simulations. Int. J. of Clim., 27, 358-371, 2007.

Kain, J. S.;Fritsch, J. M.: Convective parameterization for mesoscale models: The Kain Fritsch scheme. In: The Representation of Cumulus Convection in Numerical Models, Meteor. Monogr., Vol. 24, No. 46, pp. 165-170. American Meteorological Society, Boston, 1993.

Kaspar, F.; Cubasch, U.: Simulation of East African precipitation patterns with the regional climate model CLM, Meteorologische Zeitschrift, accepted, subject to minor revisions, 2008.

Legutke, S.,Voss, R.: The Hamburg Atmosphere-Ocean Coupled Circulation Model ECHO-G. Tech. Rep. No. 18, DKRZ, Hamburg, 1999.

Sepulchre, P., Ramstein. G., Fluteau, F., Schuster, M., Tiercelin, J.-J., Brunet. M.: Tectonic uplift and Eastern Africa aridification, Science, 313, 1419-1423, 2006.

Sun, L., Semazzi, F. H. M., Giorgi, F., Ogallo, L.: Application of the NCAR regional climate model to eastern Africa. 1. Simulation of the short rains of 1988. J. Geophy. Res., 104, D6, 6529-6548, 1999.

Tiedtke, M.:A comprehensive mass flux scheme for cumulus parameterization in large-scale models. Mon. Wea. Rev., 117, 1779-1799, 1989.

An Assessment of the Surface Radiation Budget over North America in the GEM-LAM Regional Climatemodel, Reanalysis Datasets and Satellite Based Products

Marko Markovic[1], Colin Jones[1], Katja Winger[1]
[1]*University of Quebec at Montreal*
markovic@sca.uqam.ca

In this report we evaluate the components of the surface radiation budget (SRB) from 2 sets of reanalysis data (ERA40, Uppala et al. 2005 and the NCEP-NARR, Mesinger et al., 2004) against a suite of surface observations (SO) across North America. We further use the direct surface radiation observations to evaluate the SRB derived from the ISCCP satellite dataset (Rossow and Schiffer, 1991) The surface radiation measurements consist of downwelling longwave (DLR) and solar (ISR) radiation at 6 sites across North America, coordinated by the NOAA US-SURFRAD Network (http://www.srrb.noaa.gov/surfrad/). The most accurate gridded surrogate SRB data set (reanalysis or satellite product) is subsequently used to evaluate the SRB components simulated by GEM-LAM for the recent past (1996-2002), when run at 0.5° resolution for a domain covering the entire North American continent forced by ECMWF analysed lateral and surface boundary data.

Figure 1 presents the mean annual cycle of monthly mean ISR (Fig. 1a) and DLR (Fig. 1b), averaged across all 6-measurement sites for: SO, ERA40, NARR and ISCCP along with their respective biases (Figs. 1c and 1d). NARR overestimates ISR by ~30-50 Wm^{-2} in summer and winter. These errors are considerably larger than the uncertainty of SO and are primarily due to a significant underestimate of cloud fraction in NARR which reaches as large as a 25% in the summer season (not shown). In winter, the average ISR error in ERA40 is less than 10 Wm^{-2} and in summer ~7 Wm^{-2}. The ERA40 ISR therefore appears very accurate at the 6 locations we are able to evaluate it over North America. ISCCP ISR in winter also agrees very well with SO, while in summer an overestimate of ~7 Wm^{-2} is present. The ISCCP ISR errors are therefore also close to the range of observational uncertainty. For DLR, monthly mean DJF and JJA biases are less then 5 Wm^{-2} (Figs.1b and d) in ERA40, while larger winter season biases are found in NARR (~10 Wm^{-2} underestimate) and in ISCCP (~10 Wm^{-2} overestimate). The ISCCP DLR winter errors are likely associated with the known difficulties in detecting clouds during the winter season, when the frequent presence of atmospheric inversions over a highly reflective snow surface makes satellite detection of clouds extremely difficult (Schweiger and Key, 1992). A similar comparison performed separately for the 6 SURFRAD stations revealed that the accurate ISR ISCCP values resulted, in part from the cancellation of opposite signed biases spatially across the 6 station locations (not shown), confirming ERA40 to be the most accurate surrogate SRB product over North America and an appropriate validation data set for RCM simulated SRB.

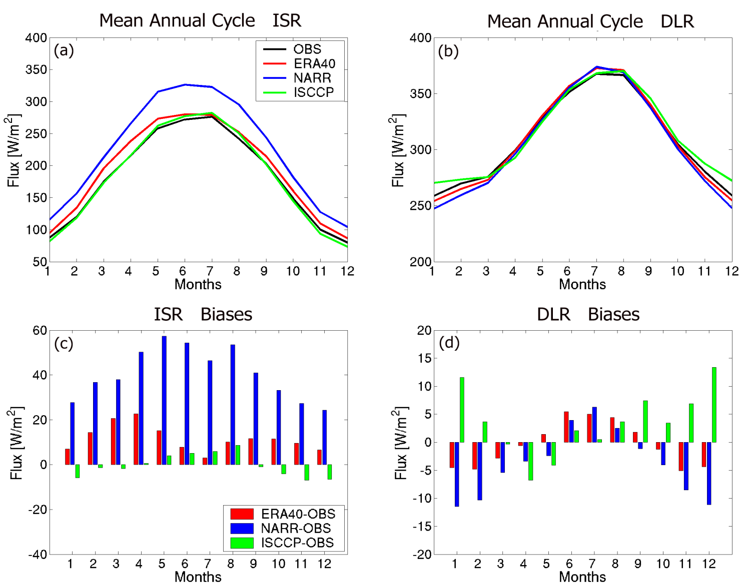

Figure 1: Mean annual cycle of: (a) ISR, (b) DLR, (c) ISR biases, (d) DLR biases. Observations are given in black, ERA40 in red, NARR in blue and ISCCP in green color.

ERA40 is therefore used to evaluate the simulated SRB in GEM-LAM for the period 1996-2002. The

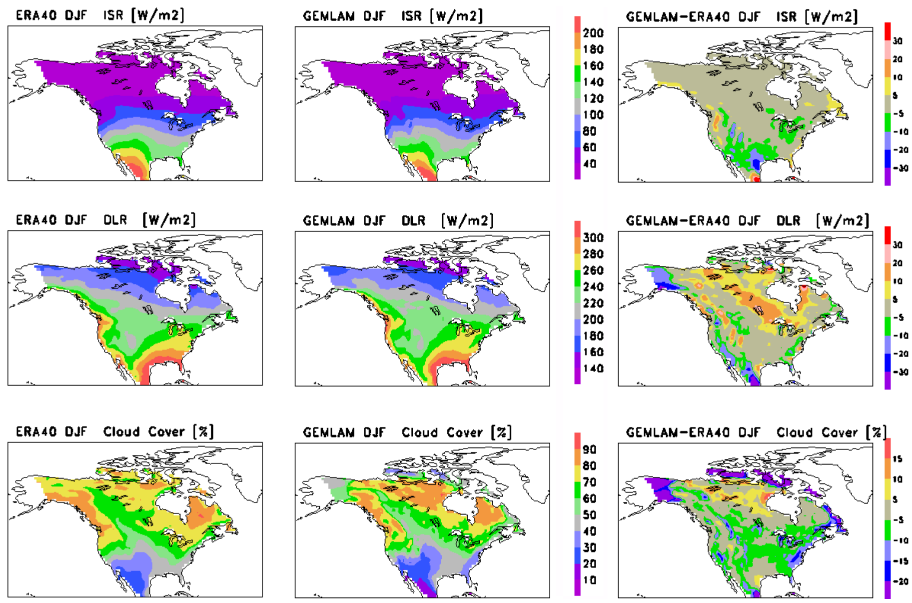

Figure: 2. Comparison of ISR, DLR and cloud cover for ERA40, GEM-LAM and their bias, winter season.

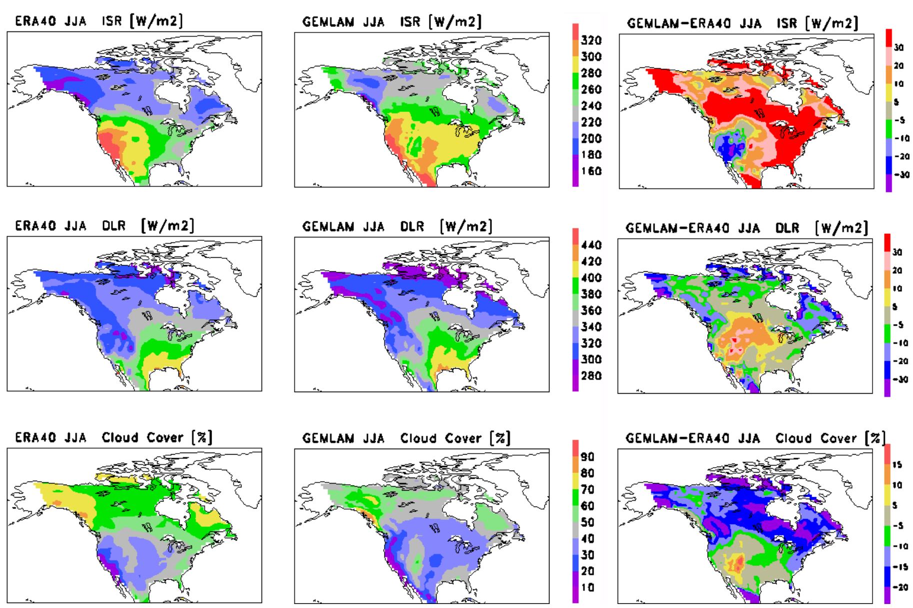

Figure: 3. Comparison of ISR, DLR and cloud cover for ERA40, GEM-LAM and their bias, summer season.

simulated DJF ISR in GEM-LAM (Fig. 2 top row) follows quite closely the ERA40 values both in terms of magnitude and spatial pattern. In the high and mid-latitudes GEM-LAM has very accurate DJF ISR while further south negative biases of ~5-10 Wm^{-2} are evident. DJF DLR in GEM-LAM also shows a similar distribution to ERA40 (Fig. 2 middle row), with biases generally in the range ±10 Wm^{-2} mostly located in the north. The bottom row in Figure 2 shows the comparison of simulated cloud cover (ERA40 and GEM-LAM). Biases may exist in the ERA40 cloud cover, hence simulated errors in the model cloud amounts should be treated with caution. Consistency between errors in cloud cover and those in surface radiation are clearly evident over Northern Canada where GEM-LAM overestimates cloud amounts, collocated with a positive bias in DJF DLR. Figure 3 shows absolute values of ERA40 and GEM-LAM ISR, DLR and cloud cover for JJA season. GEM-LAM has a positive bias in ISR (> 30 Wm^{-2}) over much of North America, which is spatially coherent with a negative bias (0 to -20 Wm^{-2}) in DLR. Both of these errors appear consistent with an underestimate of JJA cloud cover.

References: Mesinger et al., 2004: North American Regional Reanalysis. *AMS Bulletin* submitted.
Rossow and Schiffer, 1991: ISCCP cloud data products, *Bull. Am. Mel. Soc.*, **72**.
Schweiger and Key., 1992: Arctic Cloudiness: Comparison of ISCCP-C2 and Nimbus-7 Satellite derived Cloud Products with a Surface-based Cloud Climatology. *J. of Clim*: Vol. **5**,
Uppala et al., 2005: The ERA 40 re-analysis. *Q. J. R. Met. Soc*. **131**.

Regional climate simulation at 20 km using CCAM with a scale-selective digital filter

John L. McGregor, Kim C. Nguyen and Marcus Thatcher

CSIRO Marine and Atmospheric Research Melbourne 3195 Australia

1 Introduction

The CSIRO Conformal-Cubic Atmospheric Model (CCAM) has been used for a number of years for dynamical climate downscaling, mainly over the Australian region. CCAM is a variable-resolution global model. By using the Schmidt (1977) transformation, fine resolution may be achieved over any part of the globe. We have performed simulations over Australia at 60 km resolution, downscaling from NCEP reanalyses for 1951-2000, and from the CSIRO Mk 3.0 coupled GCM from 1961-2100 (McGregor et al., 2002). We have also performed long simulations at 14 km over Tasmania, Cairns and Rockhampton, and a 10-year simulation at 8 km over Fiji (Lal et al., 2008). Another 10-year simulation over Asia has also been performed (Nguyen and McGregor, 2008), driven by NCEP reanalyses. The simulations employed sea surface temperatures and sea-ice cover from the host model (or reanalysis), and typically used weak nudging from upper-level winds to provide broad similarity of storm tracks with the host model or reanalysis. The present CCAM regional climate simulation uses a C72 global grid (6 x 72 x 72 grid points), with a Schmidt stretching factor of 0.15. CCAM then achieves a fine resolution of 20 km for the central panel which is located over eastern Australia. The grid is illustrated in Figure 1. This report describes downscaling from the CSIRO Mk 3.0 coupled climate model, for model years corresponding to 1961-2000.

CCAM is an hydrostatic model, with two-time-level semi-implicit time differencing. It employs semi-Lagrangian horizontal advection with bi-cubic horizontal interpolation (McGregor, 1996), in conjunction with total-variation-diminishing vertical advection. The grid is unstaggered, but the winds are transformed reversibly to/from C-staggered locations before/after the gravity wave calculations, providing improved dispersion characteristics (McGregor, 2005b). Three-dimensional Cartesian representation is used during the calculation of departure points, and also for the advection or diffusion of vector quantities. Further details of the model dynamical formulation are provided by McGregor (2005a) and McGregor and Dix (2008). CCAM also includes a fairly comprehensive set of physical parameterizations.

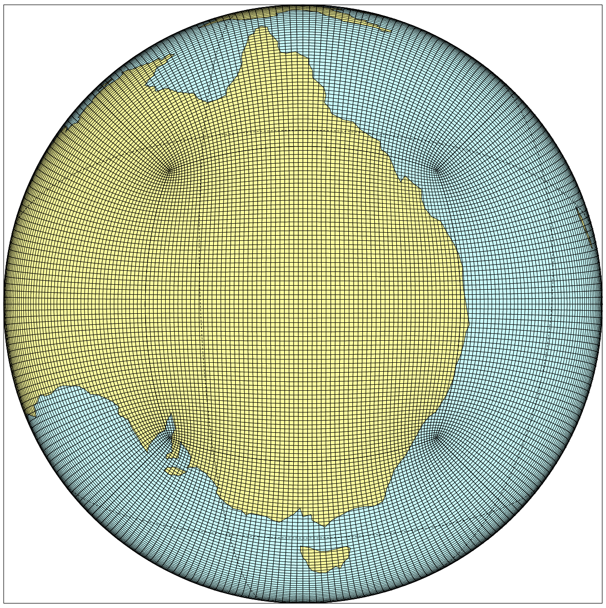

Figure 1. The C72 conformal-cubic grid used for the CCAM simulations over eastern Australia.

2 Simulation design

It should be noted that the Mk 3.0 coupled GCM does not employ flux corrections; hence there are some biases of sea-surface temperatures (SSTs), up to 2 degrees near Australia, compared to observations. The CCAM simulation uses the daily SSTs from Mk 3.0, but with the average monthly two-dimensional biases first subtracted. Sea-ice distributions are interpolated directly from the daily values of Mk 3.0.

For a prior CCAM climate simulation downscaling from NCEP reanalyses for 1951-2000, global nudging of winds above 500 hPa from the large-scale fields was employed, whilst outside the central high-resolution panel, gradually-increasing far-field nudging was also employed for MSL pressures and winds between 900 hPa and 500 hPa. This technique was adopted to help ensure that the north-south shifts of the jet-stream were captured. A new digital-filter technique, applied 12-hourly, is used in the present project, whereby "large-scale" features of MSL pressure and the winds above 500 hPa are similar to those of Mk 3.0; "large-scale" here is specified as a length scale approximately the width of New South Wales.

3 Digital filter

Thatcher and McGregor (2008) have devised an efficient approximation to the two-dimensional convolution procedure for a scale-selective Gaussian digital filter on the surface of a sphere. This approximation consists of a sequence of one-dimensional passes on the six panels of the conformal-cubic grid. The orientation of the one-dimensional passes is illustrated schematically in Figure 2.

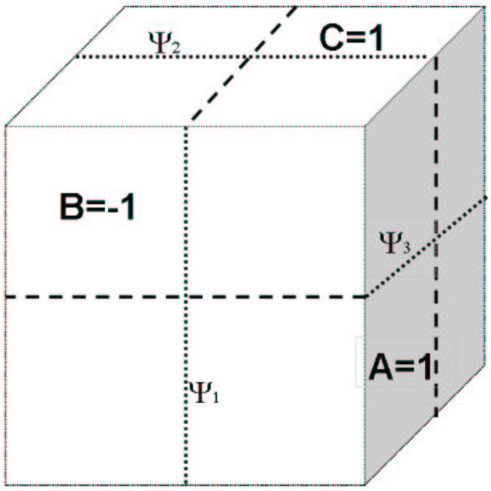

Figure 2. Schematic illustrating one-dimensional passes of the Gaussian digital-filter. Passes corresponding to the short dashed lines are performed before those with long dashed lines. A, B, and C refer to coordinate axes of the cubic geometry.

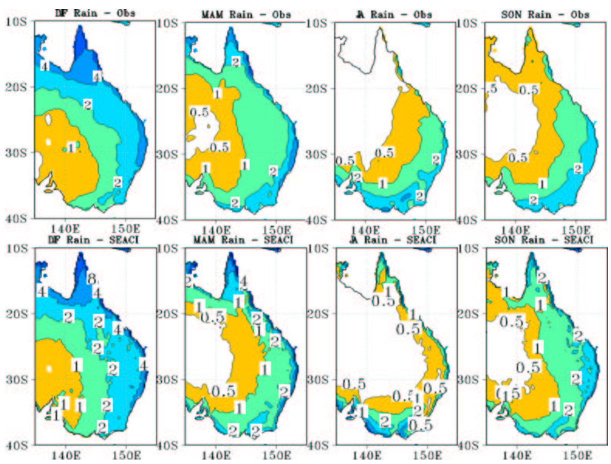

Figure 3. Seasonally-averaged rainfall (mm/day), with observations (top) and CCAM (downscaled from Mk 3.0, bottom).

4 Seasonal-mean rainfall results

The 40-year (1961-2000) monthly-mean CCAM rainfall was averaged to produce seasonal averages for December, January and February (DJF), March, April and May (MAM), June, July and August (JJA) and September, October and November (SON). These averages are compared against the observed seasonal rainfall provided by the Australian Bureau of Meteorology.

In general, CCAM reproduces the mean seasonal rainfall patterns (Figure 3). The large rainfall along the eastern coast is well captured for all seasons. The large rainfall along the Great Dividing Range and the eastern coast is also reproduced, except in winter when it is deficient. Inland of the Great Dividing Range, summer rainfall is well captured, autumn and winter are somewhat lower than observed, whereas spring rainfall is somewhat larger than observed over inland New South Wales and Queensland.

Acknowledgement

This work was supported by the South Eastern Australian Climate Initiative.

References

Lal, M., J. L. McGregor, and K. C. Nguyen, 2008: Simulation of surface air temperature and rainfall and its temporal and spatial distribution over Fiji. *Climate Dynamics*, **30**, 293–305.

McGregor, J. L., 1996: Semi-Lagrangian advection on conformal-cubic grids. *Mon. Wea. Rev.*, **124**, 1311–1322.

McGregor, J. L., 2005a: C-CAM: Geometric aspects and dynamical formulation [electronic publication]. Technical Report 70, CSIRO Atmospheric Research, 43 pp.

McGregor, J. L., 2005b: Geostrophic adjustment for reversibly staggered grids. *Mon. Wea. Rev.*, **133**, 1119–1128.

McGregor, J. L., and M. R. Dix, 2008: An updated description of the Conformal-Cubic Atmospheric Model. *High Resolution Simulation of the Atmosphere and Ocean*, K. Hamilton and W. Ohfuchi, Eds., Springer, 51–76.

McGregor, J. L., K. C. Nguyen, and J. J. Katzfey, 2002: Regional climate simulations using a stretched-grid global model. *Research Activities in Atmospheric and Oceanic Modelling Rep. 32, WMO Tech. Doc. 1105*, H. Ritchie, Ed., 3.15–3.16.

Nguyen, K. C., and J. L. McGregor, 2008: Modelling Asian summer monsoons using CCAM. *Climate Dynamics*, submitted.

Thatcher, M., and J. L. McGregor, 2008: Using a scale-selective filter for dynamical downscaling with the conformal cubic atmospheric model. *Mon. Wea. Rev.*, submitted.

Simulation of the oceanic temperatures impact on the European weather conditions

Igor I. Mokhov[1], Vladimir A. Semenov[1,2] and Vyacheslav C. Khon[1]

Obukhov Institute of Atmospheric Physics Russian Academy of Sciences
Leibniz Institute of Marine Sciences at the University of Kiel, Germany
e-mail: mokhov@ifaran.ru

Significant changes of the weather conditions over Europe in the last three decades may be linked to warming trend of the sea surface temperatures (SSTs) of the world oceans. Several model studies suggested driving role of the SST warming in tropical oceans for the atmospheric circulation trends in Atlantic-European sector [Hurrell et al. 2004; Hoerling et al. 2004]. However, not all models simulate significant changes [e.g. Schneider et al. 2003], and if they do, the response is weaker then observed changes. Another region, which directly affects the northern extratropical climate and in particular European weather conditions, is the North Atlantic (NA). The recent studies demonstrated a major role of the NA SST for hemispheric climate variability [Zhang et al. 2007; Sutton and Hodson 2007]. Multidecadal SST variability in the North Atlantic may be linked to the variations of the meridional overturning circulation, MOC [Latif et al. 2004]. Long-term oscillations of the MOC provide predictability potential for the decadal SST changes and possible response of the European climate.

Here, we investigate the atmospheric response to prescribed SSTs and sea ice concentrations for two periods related of colder and warmer SSTs in the North Atlantic (Figure 1), which may represent low and high MOC circulation intensity [Latif et al. 2004]. Two simulations of 100 year duration with the ECHAM5 model at T42 resolution (~2.8°x2.8° lat/lon) were performed using climatological SST/sea ice boundary conditions (see Fig. 1). Simulated differences for surface air temperature (SAT) and sea level pressure (SLP) are presented in the Figure 2. The moderate warming is simulated over Europe with stronger changes over south-western part. The changes in summer season exceed those for the winter and reach 1.5 °C over Spain. Significance test has shown that summer changes are more detectable. This is in line with results by [Sutton and Hodson 2007] who found summer time response to be more robust than for the winter time. The SLP changes, however, are stronger in the winter season with statistically significant low pressure anomaly centered around 50E-50N. This anomaly is very similar to the observed feature as present in the NCEP/NCAR reanalysis data (not shown) and may be due to strong sea ice reduction in the Barents Sea, which accompanied the NA SST warming.

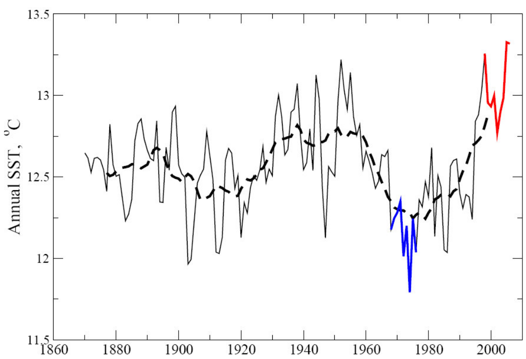

Figure 1: annual SST in the (50W-10W, 40N-60N) box in the NA (see Latif et al. 2004). Two climatologies of the SST and ice extent for the periods indicated by blue and red were used as boundary conditions for model simulations.

The work is supported by Russian Ministry of Sciences and Education and Russian Foundation for Basic Research.

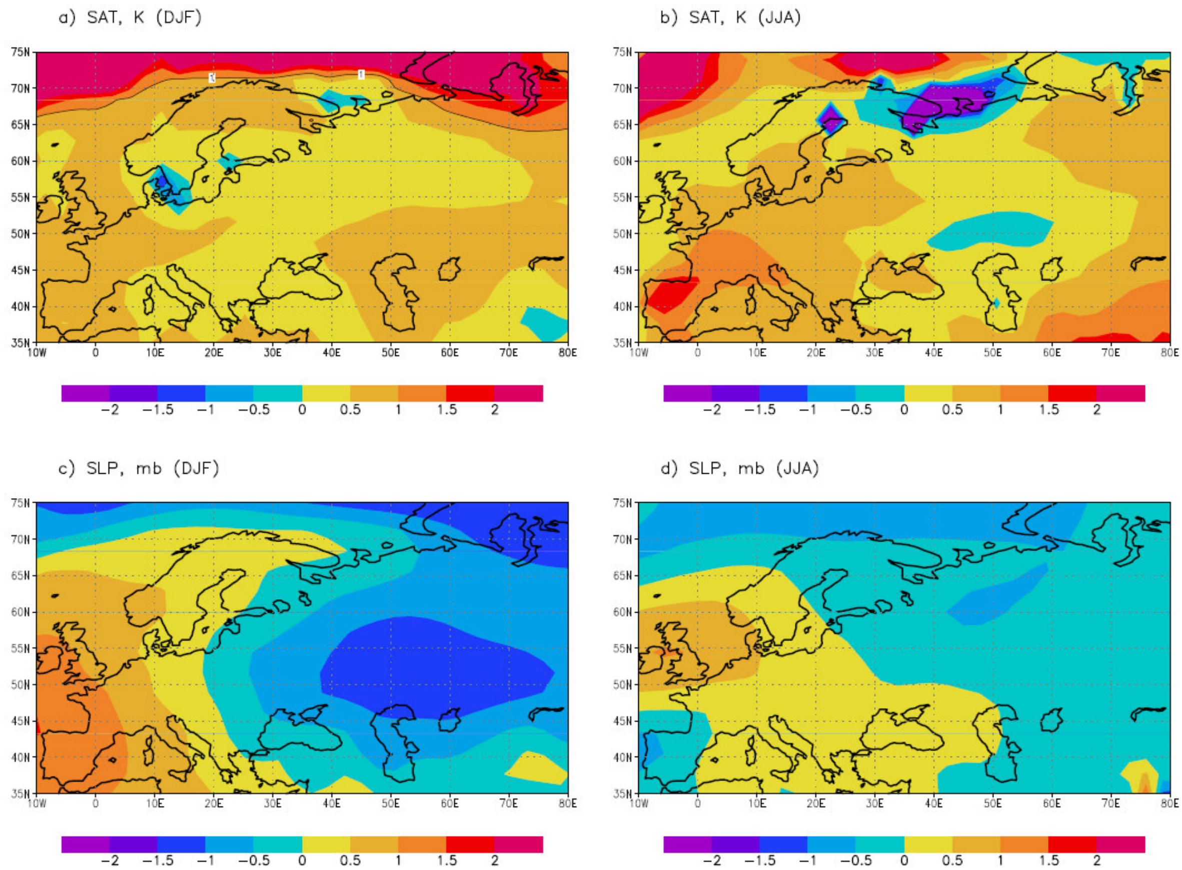

Figure 2: Simulated changes of the SAT and SLP for winter and summer between “warm” and “cold” North Atlantic numerical experiments.

References

Hoerling, M. P., Hurrell, J. W., Xu, T., Bates, G. T., and A. S. Phillips (2004), Twentieth century North Atlantic climate change. Part II: Understanding the effect of Indian Ocean warming, *Climate Dyn.*, *23*, 391-405.

Hurrell, J.W., Hoerling, M.P., Phillips, A.S., and T. Xu, Twentieth century North Atlantic climate change. Part 1: assessing determinism, Clim. Dyn., 23, 371-389, 2004.

Latif, M., Roeckner, E., Botzet, M., Esch, M., Haak, H., Hagemann, S., Jungclaus, J., Legutke, S., Marsland, S., Mikolajewicz, U., Mitchell, J. Reconstructing, monitoring, and predicting multidecadal-scale changes in the North Atlantic thermohaline circulation with sea surface temperature // J. Climate. 2004. V. 17. № 7. P. 1605-1614.

Roeckner, E., et al. (2003), The atmospheric general circulation model ECHAM 5. Part I: Model description, *Rep. 349*, Max Planck Inst. For Meteorol., Hamburg, Germany.

Sutton, R.T., and D.L. Hodson (2007) Climate Response to Basin-Scale Warming and Cooling of the North Atlantic Ocean, J. Climate, 20, 891-907.

Schneider, E. K., Bengtsson, L., and Z.-Z. Hu (2003), Forcing of Northern Hemisphere climate trends, *J. Atmos. Sci., 60*, 1504–1521.

Zhang, R., Delworth, T.L., and I. M. Held (2007) Can the Atlantic Ocean drive the observed multidecadal variability in Northern Hemisphere mean temperature? Geophys. Res. Lett., 34, L02709, doi:10.1029/2006GL028683.

Geoengineering efficiency: Preliminary assessment with a climate model of intermediate complexity

I.I. Mokhov and A.V. Eliseev

A.M. Obukhov Institute of Atmospheric Physics RAS,
3 Pyzhevsky, 119017 Moscow, Russia, e–mail: mokhov@ifaran.ru

Recently, a renewed interest appeared in an emploiment of the M.I. Budyko's [3] suggestion to load sulphur particles in the stratosphere to enhance the Earth's albedo and to mitigate the global warming, an approach of geoengineering [7, 4, 9]. In the present paper, the climate model of intermediate complexity developed at the A.M. Obukhov Insitute of Atmospheric Physics RAS (IAP RAS CM) [8] is used to estimate geoengineering efficiency to mitigate climate changes.

In the IAP RAS CM, the value of extinction coefficient $k_{e,strat}$ for stratospheric sulphates is derived from estimations for the Mt. Pinatubo eruption in 1991. During this eruption, total loading of sulphates in the stratosphere is estimated to be 10 TgS [1] and maximum global mean optical depth for volcanic aerosols is estimated to be close to 0.15 [6]. This leads to $k_{e,strat} = 7.6\ m^2/gS$.

A simulation is performed with the IAP RAS CM forced by the anthropogenic emissions of CO_2 and CH_4 (their concentrations are computed interactively in the model by modules forcarbon and methane cycles) and atmospheric concentration of N_2O and sulphate aerosols in accordance to historical data for the 19th–20th centuries and in accordance to scenario SRES A1B for the 21st century. More detailed description of these forcing scenarios is reported in [5].

Without a geoengineering mitigation, near–surface atmosphere warms by about 2.8 K till the end of the 21st century with respect to the equilibrated preindustrial state, and by about 2.1 K with respect to the late 20th century.

For a geoengeenering mitigaton, local concentratation of stratospheric sulphates is computed as a product of their gloobal loading $M_{geoeng,g}$ and a prescribed latitudinal profle$f(\phi)$. This distribution is chosen either uniform or triangular with respect to sine of latitude (with zeroes at the North and South Poles and with a maximum at a prechosen latitude $\phi_{m,1}$ varying between $50^o S$ and $70^o N$) or trapesoidal (with zeroes at the North and South Poles and a with flat maximum in the latitudinal range $\phi^o_{m,2} S - \phi^o_{m,2} N$; $\phi_{m,2} = 0^o - 70^o$). Global loading of anthropogenic stratospheric sulphates is modelled by solving equation

$$\frac{dM_{geoeng,g}}{dt} = E_{geoeng,g} - \frac{M_{geoeng,g}}{\tau_{strat}}$$

where global geoengineering emissions $E_{geoeng,g}$ amount $1 - 2\ TgS/yr$ [4, 9] starting from year 2012 and equal to zero before this date. The lifetime of stratospheric sulphates τ_{strat} is set to 2 yr [7].

After a geoengineering emissions start, difference in globally and annually averaged surface air temperature, $\Delta T_{geoeng,g}$ between the simulation pairs with and without geoengineering emissions becomes stationary within few decades and changes only marginally after 2050's. For $E_{geoeng,g} = 1\ TgS/yr$ ($E_{geoeng,g} = 2\ TgS/yr$) in the late 21st century it amounts $0.07 - 0.11\ K$ $(0.13 - 0.22\ K)$ depending on $f(\phi)$ and scaling linearly between different values of $E_{geoeng,g}$.

To assess the sensitivity of the obtained results to this value, $k_{e,strat}$ varied in additional simulations between 5 m^2/gS and 10 m^2/gS in the performed simulations with the IAP RAS CM. In this, respective ranges of $\Delta T_{geoeng,g}$ widen to $0.04 - 0.15\ K$ $(0.09 - 0.30\ K)$.

Among the mentioned above $f(\phi)$, the most effective latitudinal distribution of aerosol loading is either triangular with $\phi_{m,1}$ in the range beteen $50^o N$ and $70^o N$ or uniform distribution. The least effective are trapesoidal distributions especially that with $\phi_{m,2} = 30^o$. In terms of $\Delta T_{geoeng,g}$, geoengineering efficiency differs between the most and the least effecitve $f(\phi)$ by a factor of 1.5.

According to the obtained results, it is possible to slow down current anthropogenic warming by applying geoengineering approach. However, the residual warming is still substantinal. For the SRES A1B scenario this residual warming in the 21st century is estimated to be greater than 1.8 K.

This work is supported by the Russian Foundation for Basic Research, by the programs of the Russian Academy of Sciences, and by the Russian President scientific grant.

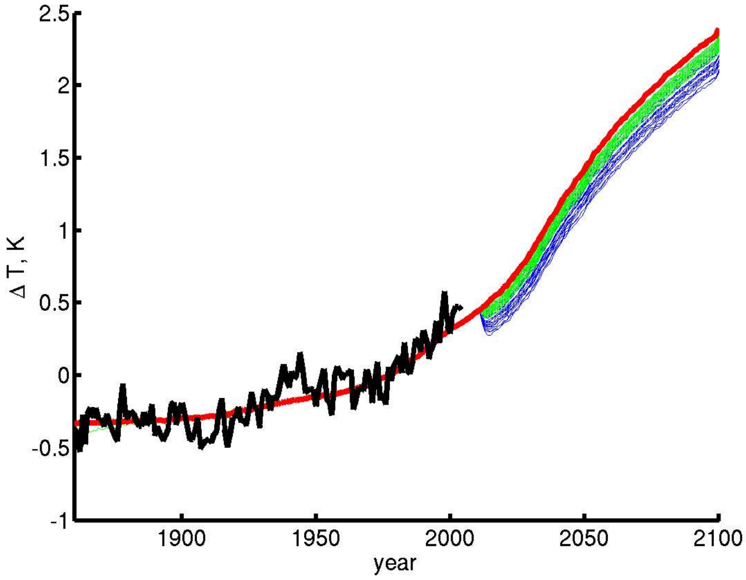

Figure 1: Change of globally and annually averaged surface air temperature as simulated by the IAP RAS CM with the combined anthropogenical historical+SRES A1B forcings in comparison to the observations [2] (black line) greenhouse gases and sulphate aerosol forcings (red curve) and geoengineering ensembles for $E_{geoeng,g} = 1\ TgS/yr$ and $E_{geoeng,g} = 2\ TgS/yr$ (green and blue lines respectively).

References

[1] G.J.S. Bluth, S.D. Doiron, C.C. Schnetzler, A.J. Krueger, and L.S. Walter. Global tracking of the SO2 clouds from the June, 1991 Mount Pinatubo eruptions. *Geophys. Res. Lett.*, 19(2), 1992.

[2] P. Brohan, J.J. Kennedy, I. Harris, S.F.B. Tett, and P.D. Jones. Uncertainty estimates in regional and global observed temperature changes: A new data set from 1850. *J. Geophys. Res.*, 111(D12):D12106, 2006.

[3] M.I. Budyko. *Climate Changes*. Gidrometeoizdat, Leningrad, 1974. [English transl. published in 1977 by the American Geophysical Union, Washington, D.C.].

[4] P.J. Crutzen. Albedo enhancement by stratospheric sulfur injections: A contribution to resolve a policy dilemma? *Clim. Change*, 77(3-4):211–219, 2006.

[5] A.V. Eliseev, I.I. Mokhov, and A.A. Karpenko. Influence of direct sulfate–aerosol radiative forcing on the results of numerical experiments with a climate model of intermediate complexity. *Izvestiya, Atmos. Ocean. Phys.*, 42(5):544–554, 2007.

[6] J. Hansen, M. Sato, L. Nazarenko, R. Ruedy, A. Lacis, D. Koch, I. Tegen, T. Hall, B. Shindell, D. Santer, P. Stone, T. Novakov, L. Thomason, R. Wang, Y. Wang, D. Jacob, S. Hollandsworth, L. Bishop, J. Logan, A. Thompson, R. Stolarski, J. Lean, R. Willson, S. Levitus, J. Antonov, N. Rayner, D. Parker, and J. Christy. Climate forcings in Goddard Institute for Space Studies SI2000 simulations. *J. Geophys. Res.*, 107(D18):4347, 2002.

[7] Yu.A. Izrael. An efficient way to regulate global climate is the main goal of the climate problem solution. *Rus. Meteorol. Hydrol.*, 30(10):1–4, 2005.

[8] I.I. Mokhov, V.A. Bezverkhnii, A.V. Eliseev, and A.A. Karpenko. Model estimates of global climatic changes in the 21st century with account for different variation scenarios of solar activity. *Doklady Earth Sci.*, 411(8):1327–1330, 2006.

[9] T.M.L. Wigley. A combined mitigation/geoengineering approach to climate stabilization. *Science*, 314(5798):452–454, 2006.

Climate simulations by the IAP RAS model of intermediate complexity with an implemented ocean general circulation module

Muryshev K.E., Eliseev A.V., Mokhov I.I.

A.M. Obukhov Institute of Atmospheric Physics RAS, Moscow, Russia
kmuryshev@ifaran.ru

The climate model of intermediate complexity developed at the A. M. Obukhov Institute of Atmospheric Physics RAS (IAP RAS CM) has been comprehensively described in (Petoukhov et al., 1998; Handorf et al., 1999; Mokhov et al., 2005). It includes modules for the redistribution of shortwave and longwave radiation, convection, cloud and precipitation formation. Large-scale atmospheric and oceanic dynamics (with scales larger than those corresponding to synoptic processes) are resolved explicitly. The synoptic-scale processes are treated as Gaussian ensembles. Sea ice in the IAP RAS CM is diagnosed based on surface air and sea surface temperatures. In the model version used here, surface hydrology is prescribed. The IAP RAS CM horizontal resolution is 4.5°×6° with 8 vertical layers in the atmosphere (up to 80 km). Here, the statistical-dynamical oceanic model previously used in the IAP RAS CM is replaced by oceanic general circulation model developed at the Institute of Numerical Mathematics RAS was used. The spatial resolution of the new oceanic module is 3°×5° with 25 vertical layers. Correction of heat and impulse fluxes between atmosphere and ocean in coupled model is not applied for the new version of the IAP RAS CM.

Numerical experiments with the initial and boundary conditions corresponding to the present climate and to the doubled concentration of carbon dioxide in the atmosphere have been carried out. All basic atmospheric and oceanic fields obtained in the first numerical simulations are in general agreement with the corresponding observed data. The simulated globally and annually averaged surface air temperature is 13.5°C, while the observational value is 14°C (Brohan et al., 2006). Geographical distribution of surface air temperature is also close to observations. Most marked deficiencies are found in Antarctic and North-Atlantic regions, on the coast of Barents Sea and over Africa.

In the previous model version, doubling of the CO_2 atmospheric content caused globally averaged surface air temperature rise about 2.2 K. In the present version, this increase amounts 2.8 K. Corresponding estimations with different state-of-the-art models are in the range 1.8 – 4.5 K.

References

Brohan P., Kennedy J.J., Harris I., Tett S.F.B. and Jones P.D., 2006: Uncertainty estimates in regional and global observed temperature changes: a new dataset from 1850. *J. Geophys. Res.*, **111**, D12106.

Handorf D., Petoukhov V.K., Dethloff K., Eliseev A.V., Weisheimer A., Mokhov I.I., 1999: Decadal climate variability in a coupled atmosphere-ocean climate model of moderate complexity. *J. Geophys. Res.*, **104**, N.D22. 27253-27275.

Mokhov I.I., Eliseev A.V., Demchenko P.F., Khon V.Ch., Akperov M.G., Arzhanov M.M., Karpenko A.A., Tikhonov V.A., Chernokulsky A.V., Sigaeva E.V., 2005: Climate Changes and Their Assessment Based on the IAP RAS Global Model Simulations. *Doklady Earth Sciences*, **402**, No. 4, 591-595.

Petoukhov V.K., Mokhov I.I., Eliseev A.V., Semenov., 1998: The IAP RAS Global Climate Model: V.A. Moscow: Dialogue-MSU, 110 p.

Annual mean surface air temperature from simulations [^{o}C]

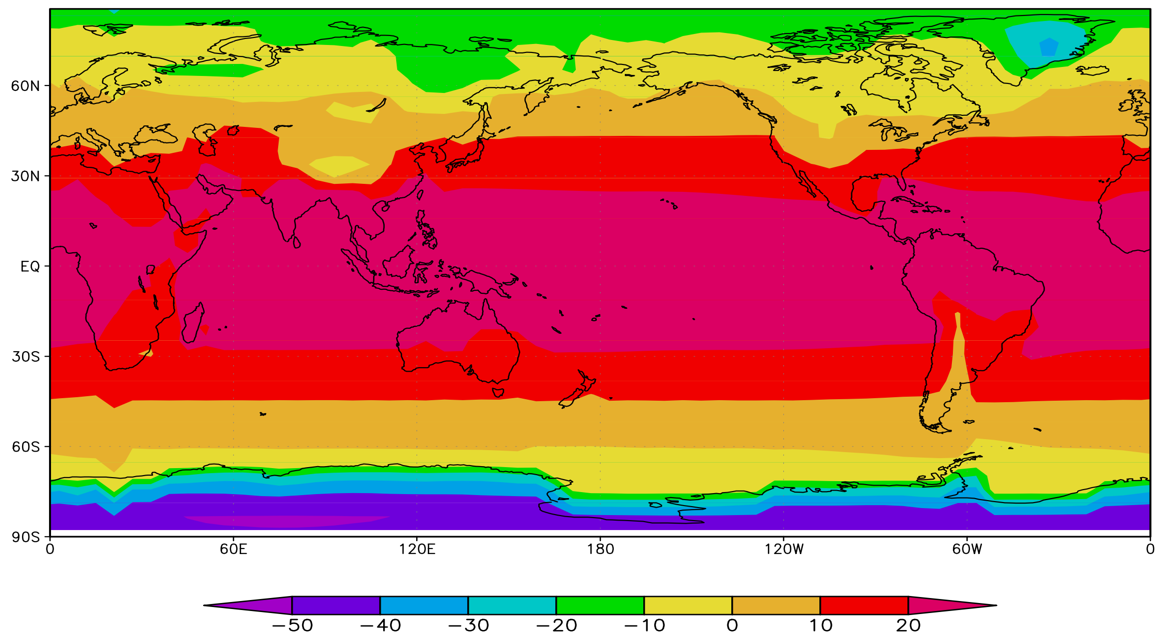

Annual mean surface air temperature from observations [^{o}C]

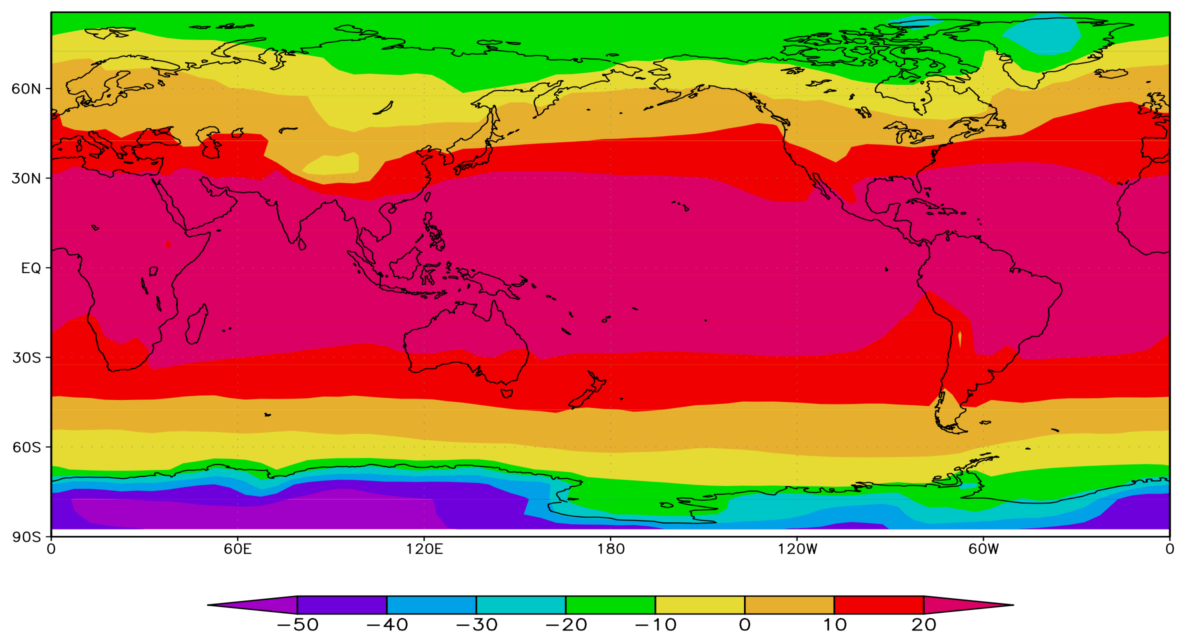

Comparison of the Cloud-Radiation Interaction between GEM and ARM-SGP Observations

Danahé Paquin-Ricard[1], Colin Jones[1], Paul Vaillancourt[2]
[1]CRCMD, Université du Québec à Montréal, [2]Environment Canada
danahe@sca.uqam.ca

Introduction

Microphysical processes play a key role in controlling the liquid and ice water content of simulated clouds and, as a result, are important controls on the interaction of clouds with both solar and terrestrial radiation. Due to their extreme complexity, processes controlling the cloud-radiation interaction are highly parameterized in present-day climate models. Here, we evaluate the cloud-radiation interaction as simulated by the new Canadian Regional Climate Model, based on the limited area version of GEM (Global Environmental Multi-scale Model, [1]). We evaluate the simulated co-variability of downwelling shortwave (SWD) and longwave (LWD) radiation at the surface as a function of liquid water path (LWP) and integrated water vapor (IWV).

Model and Observations

Observations comes from the ARM (http://www.archive.arm.gov) Southern Great Plains (SGP) site, at the central facility (CF-1). Data streams used for this model evaluation are the *improved MicroWave Radiometer RETrievals of cloud liquid water and precipitable water vapor* (MWRRET) with LWP and IWV derived from the 2-channel microwave radiometer and the *surface RADiation measurement (BEFLUX input) Quality Control testing* (QCRADBEFLUX1LONG) which provides observed downwelling SWD and LWD radiation at the surface.

GEM uses a prognostic total cloud water variable, with a Sundqvist-type, bulk-microphysics scheme. GEM-LAM was integrated for the period 1998-2004 over a domain centered on the ARM-SGP site CF-1 (37°N, 97 °W). The integration used ECMWF reanalysis as lateral boundary conditions, prescribed SSTs and employed a horizontal resolution of $\sim$ 42 km. Time series of model results were extracted from the grid-point closest to the ARM-SGP site.

Both observations and model are averaged over 3 h periods for the entire 7 years. The MWR cannot operate when its teflon window is wet. For this reason, all precipitation events greater than 0.25 mm/3h are removed from the data-set of LWP and IWV for both observations and model.

Results

In this section, we present the summer (JJA) and winter (DJF) co-variability graphs. Observations are in blue and model is in red. In order to isolate the IWV effect on downwelling radiation, only clear sky conditions (cloud fraction $\leq$10 %) are used for the SWD-IWV and LWD-IWV co-variability. Similarly, only cloudy sky conditions (cloud fraction $\geq$90 %) are used for SWD-LWP and LWD-LWP co-variability.

In the following figures (A-D), SWD is divided by the cosine of the local solar zenith angle (SZA). Shown are only values for SZA below 65° for figures A-B and for SZA below 85° for figures C-D.

Figures A and B show the interaction between SWD and IWV for JJA and DJF respectively. GEM reproduces well this interaction during the summer but has a negative bias during the winter. In other words, GEM underestimates downwelling SWD at surface for a given amount of IWV compared to observations. Figures C and D depict the interaction between SWD and LWP for JJA and DJF respectively. They show that the model reproduces fairly well the observed interaction between LWP and SWD except for an overestimation in SWD for low amount of LWP during the summer.

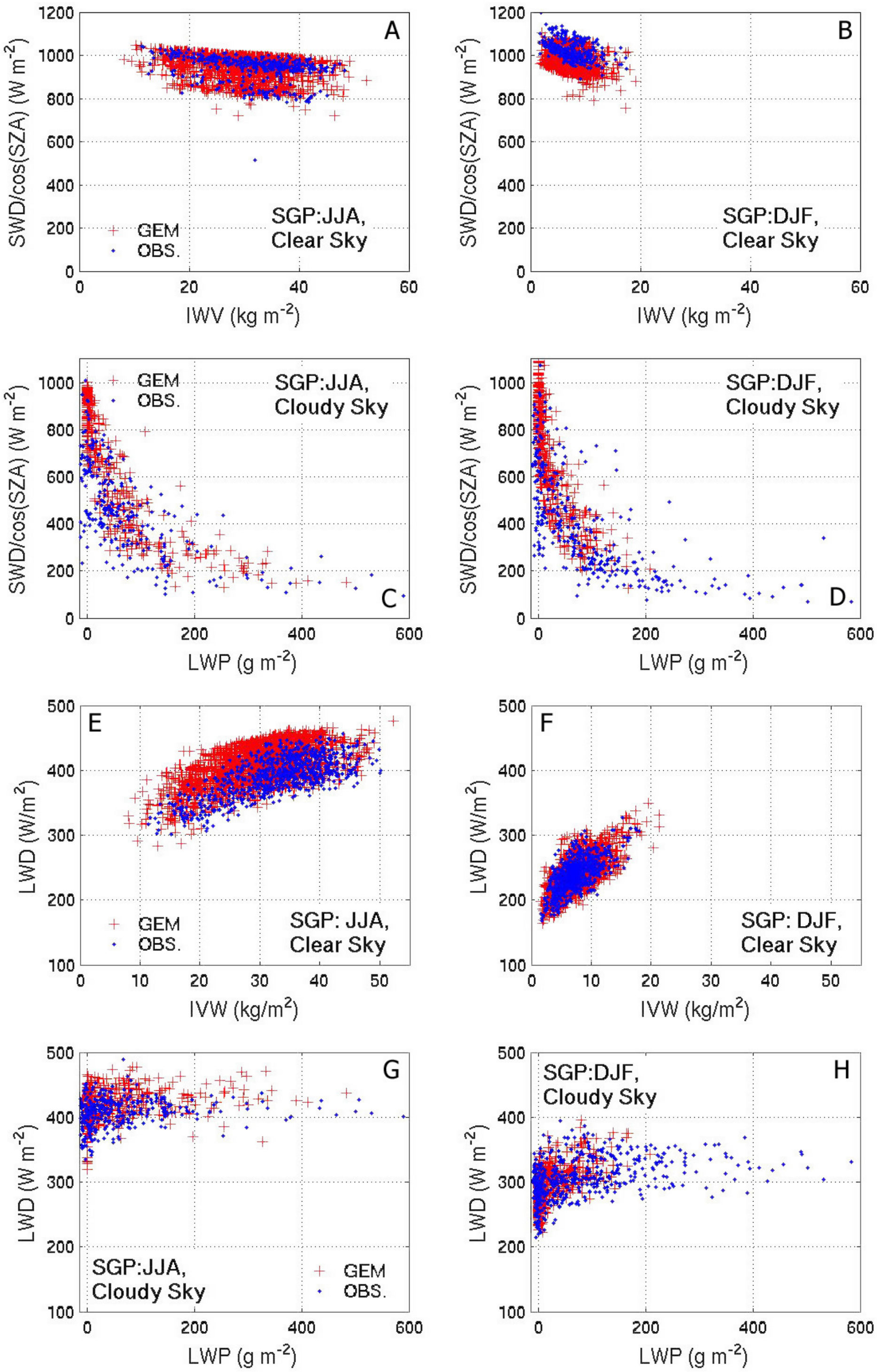

Figures E and F show the interaction between LWD and IWV for JJA and DJF respectively. The model reproduces well the observed interaction except for a positive bias during the summer, result of a warm temperature bias during that season at this particular site. For the LWD-LWP interaction, figures G and H show that the cloud emissivity is saturated through the LWP range of observations. GEM reproduces well this interaction except for the same positive bias in the summer season as shown by figure E.

Conclusions

From these results, we conclude that GEM reproduces fairly well the cloud-radiation interaction at the SGP site except for the negative bias in winter for the SWD-IWV interaction. Without the warm temperature bias in the summer season, GEM would better reproduce the atmospheric water LWD emissivity. Furthermore, it shows that an error in simulated LWP would lead to an incorrect simulated SWD radiation at the surface but would not have an impact on the simulated LWD radiation at the surface.

Acknowledgements: Data were obtained from the ARM Program sponsored by the U.S. DOE. (www.arm.gov)

References

[1] Côté J., et al., 1998. The operational CMC-MRB global environmental multi-scale (GEM) model. Part I: Design considerations and formulation. Mon. Weather Rev.: 126, 1373-1395.

An Evaluation of Cloud and Radiation Processes Simulated by GEM-LAM for the Arctic SHEBA Year

Dragan Simjanovski, Eric Girard, Colin Jones, Ping Du
Department of Earth and Atmospheric Sciences, UQAM, Montreal, Qc.
dragan@sca.uqam.ca

Due to the unique conditions prevailing in the Arctic (e.g. extreme low temperature and water vapor mixing ratios, highly reflective sea-ice/snow surfaces, low-level inversions and the absence of solar radiation for extended periods) the macro physical and microphysical processes controlling cloud formation and cloud-radiation interactions are complex. The difficulty of simulating these processes was recently highlighted during the Arctic Regional Climate Model Intercomparison Project (ARCMIP). The objective of this study is to evaluate the new Canadian Regional Climate Model (the limited area version of the Global Environmental Multiscale model (GEM-LAM)) for the period September 1997 to October 1998 over the Western Arctic Ocean. This period was coincident with the Surface Heat Budget of the Arctic Ocean (SHEBA) field experiment. Surface downwelling shortwave (SWD) and longwave (LWD) radiation, surface albedo (SFC albedo), vertically integrated water vapor, liquid water path (LWP) and cloud cover simulated by GEM-LAM are evaluated against the SHEBA observation data. GEM-LAM is also compared to the eight other ARCMIP participating models.

The simulation domain is approximately the same as the one used during ARCMIP and covers Alaska, the Beaufort and Chukchi Seas and the Western Arctic. The simulation covers the period of September 1st 1997 to August 31st 1998 with a one-year spin-up. Initial and boundary conditions are provided by the ERA40 re-analysis and the Atmospheric Model Intercomparison Project 2 (AMIP2) for sea ice cover and sea-surface temperature.

Figure 1 shows that, in general, all models represent reasonably well the annual cycle of LWD with a maximum during summer and minimum during winter. Most models tend to underestimate LWD throughout the year. However, GEM reproduces quite well this variable with the largest underestimation during January 98 with a relative error of 10% (~-14 Wm^{-2}) and an overestimation in April 98 with a relative error of 7% (~+9 Wm^{-2}).

The inter-model spread is much larger for SWD. The intensity and time of maximum insolation substantially vary between models. GEM reproduces the SWD peak in June 1998, which is not the case for some other models with a simulated SWD peak earlier in May. GEM is also very close to observations with the largest error occurring in May 98 with a small relative error of 9% (~22 Wm^{-2}) with respect to observations.

The observed vertically integrated water vapor (figure 1c) reflects the annual cycle of temperature: low in winter and high in summer. Most models reproduce the observed annual cycle of this variable quite well. GEM-LAM tends to underestimate the vertically integrated water vapor during winter and overestimate during summer. This is likely to be related to a warm atmospheric bias in summer and a cold atmospheric bias during summer.

Observed surface albedo is around 0.70 during winter and decreases significantly during summer down to 0.35 in August 1998. GEM - LAM overestimates the surface albedo for all seasons in this experiment. It has the largest overestimation in June 1998 with relative error of 33%. The presence of melt pounds and leads, which are not considered in the simulation, is probably a factor explaining the large albedo differences between models and observations.

Observations show that cloud cover is approximately 50% during winter and 95% during summer with a steep increase (decrease) during spring (autumn). Most of the participating models are unable to capture both the annual cycle and absolute values of cloud cover. GEM systematically overestimates cloud cover during winter (September 97 – April 98). The model underestimation of winter clouds can be related to the difficulties of observing optically thin clouds in the Arctic during winter (Wyser and Jones, 2005). When these thin clouds are filtered out, the simulated cloud cover is much closer to satellite observations as shown on Figure 1e.

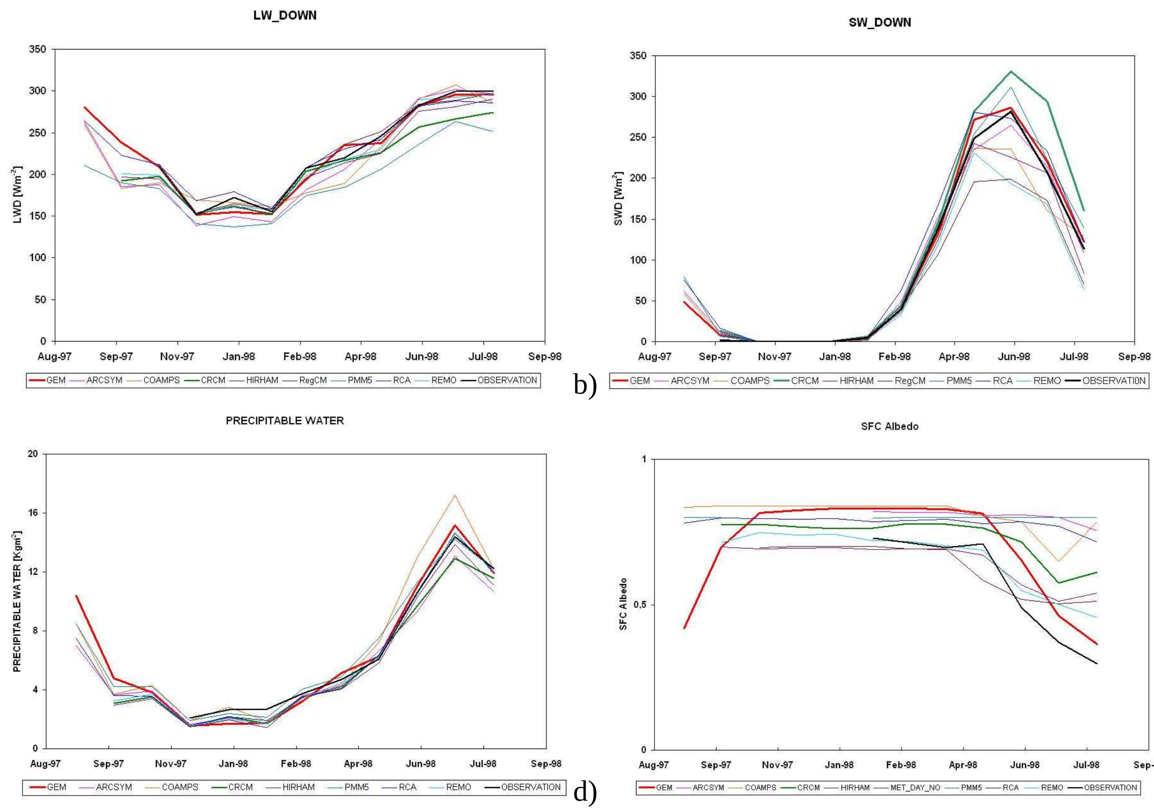

a) b) c) d)

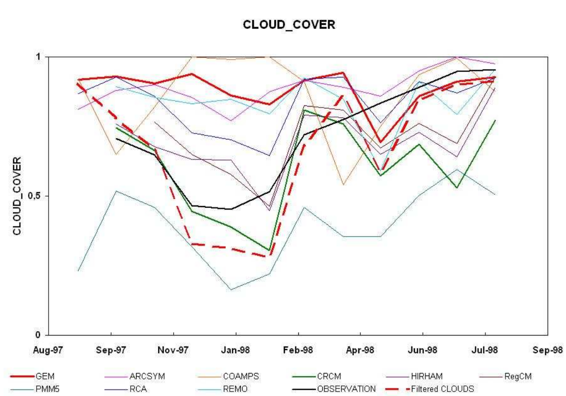

e)

Figure 1: Monthly mean of surface downwelling longwave (a) and shortwave (b) radiation, precipitable water (c), surface albedo (d) and cloud cover (e). Model GEM-LAM is presented with red line, other participating models in ARCMIP are presented with lines of different colors and SHEBA observation with black line.

References:

Wyser, K. 2007 : An Evaluation of Arctic Cloud and Radiation processes during the SHEBA year: Simulation results from 8 Arctic Regional Climate Models.

Rinke, A. 2004 : Climate Dynamics: Evaluation of an Ensemble of Arctic Regional Climate Models: Spatial Patterns and Height Profiles

Klaus Wyser, Colin G. Jones; 2005; Journal of geophysical research; Modeled and observed clouds during Surface Heat Budget of the Arctic Ocean (SHEBA); vol 110